Nanoscale Magnetic Resonance Spectroscopy Using a Carbon Nanotube Double Quantum Dot

Wanlu Song,[1,2] Tianyi Du,[1] Haibin Liu,[1,2,*] Martin B. Plenio,[2,3] and Jianming Cai[1,2,†]

[1] *School of Physics, Huazhong University of Science and Technology, Wuhan 430074, China*

[2] *International Joint Laboratory on Quantum Sensing and Quantum Metrology, Huazhong University of Science and Technology, Wuhan 430074, China*

[3] *Institut für Theoretische Physik & IQST, Universität Ulm, Albert-Einstein Allee 11, D-89081 Ulm, Germany*

(Received 15 August 2018; revised manuscript received 21 August 2019; published 11 November 2019)

Quantum sensing exploits fundamental features of quantum mechanics and quantum control to realise sensing devices with potential applications in a broad range of scientific fields ranging from basic science to applied technology. The ultimate goal are devices that combine unprecedented sensitivity with excellent spatial resolution. Here, we propose an new platform for all-electric nanoscale quantum sensing based on a carbon nanotube double quantum dot. Our analysis demonstrates that the platform can achieve sensitivities that allow for the implementation of single-molecule magnetic resonance spectroscopy and therefore opens a promising route towards integrated on-chip quantum-sensing devices.

DOI: 10.1103/PhysRevApplied.12.054025

I. INTRODUCTION

Quantum systems embodying fundamental quantum features offer an appealing perspective in sensing and metrology [1–4]. Ultra-small quantum sensors provide the possibility for locating them in very close proximity to the target to realise strong sensor-target interaction. This facilitates sensing with both ultra-high measurement sensitivity combined with a nanoscale resolution thus allowing for the identification of nanoscale objects or the detection of signals carrying, for example, magnetic information of nanostructures. The thereof emerging technology of nanoscale magnetic resonance spectroscopy provides a versatile experimental tool to investigate a wide range of physical, chemical, and biophysical phenomena in minute sample volumes [5–15].

There are two key challenges for the implementation of nanoscale magnetic resonance spectroscopy. First, the smallest possible probe-target distance is generally limited by the size of the quantum sensor. Remarkably, nanoscale quantum sensors based on the nitrogen-vacancy (N-V) center in diamond [16–18] can achieve sizes of a few nanometers. However, perturbations from the surface then start to significantly affect its sensing capabilities thus limiting further miniaturization [19–22]. Secondly, a scalable architecture of an integrated on-chip quantum-sensing device represents fundamental progress in the development of nanoscale magnetic resonance spectroscopy with appealing practical applications.

In this work, we address both challenges and propose a new type of quantum sensor based on a valley-spin qubit of a carbon nanotube double quantum dot [23–30] aiming for on-chip nanoscale magnetic resonance spectroscopy. By applying continuous electrical driving on a double quantum dot, the system can efficiently identify the frequency of weak external signals. Due to the nanometer diameter of single-walled carbon nanotubes, the valley-spin quantum sensor can be brought extremely close to the target, which promises ultra-high sensitivity. Our detailed analysis based on realistic experimental parameters demonstrates that such a carbon nanotube quantum sensor is able to identify the species of individual external nuclei, thus going well beyond both the detection of external ensembles of nuclei [31] and the detection of a single strongly coupled intrinsic nucleus [32], and thereby provides an alternative platform for nanoscale magnetic resonance spectroscopy. The system can be controlled coherently [33,34] and efficiently readout [35,36] electrically. Such all-electric manipulation without requiring optical elements facilitates the integration of on-chip carbon nanotube quantum-sensor arrays [37]. The present result is expected to extend the scope of quantum technologies based on a carbon nanotube double quantum dot system from quantum-information processing to nanoscale magnetic resonance spectroscopy.

II. MODEL OF A NANOTUBE QUANTUM SENSOR

Our quantum sensor is based on a carbon nanotube double quantum dot, as shown in Fig. 1(a). In a single-wall

*liuhb@hust.edu.cn
†jianmingcai@hust.edu.cn

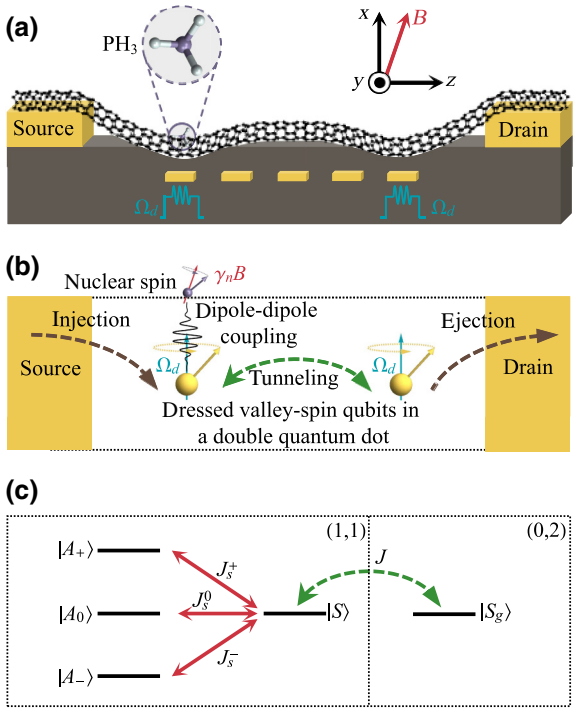

FIG. 1. Nanotube quantum sensor for nanoscale magnetic resonance spectroscopy. (a) Model of a (bent) nanotube quantum sensor for nanoscale magnetic resonance spectroscopy (a PH_3 molecule shown as an illustrative example). Five local gate electrodes create an electrically driven double quantum dot and control the electron tunneling rates [33,34]. (b) Mechanism of a nanotube quantum sensor. Both electrons are electrically driven with a Rabi frequency Ω_d, the magnetic dipole-dipole coupling between one electron spin and the external target spin (with a Larmor frequency $\gamma_n B$) lifts the Pauli blockade, see (c), and leads to a resonant leakage current when $\Omega_d = \gamma_n B$. (c) Due to a change in the local environment of the left or right quantum dot, Pauli blockade is lifted by three additional tunneling channels as denoted by $|A_{0,\pm}\rangle \leftrightarrow |S\rangle \leftrightarrow |S_g\rangle$ with the corresponding tunneling rates $J_S^{0,\pm}$ and J.

carbon nanotube, an electron has two angular-momentum quantum numbers, arising from spin and orbital motions. The orbital motion has two flavors known as the K and K' valleys, which correspond to the clockwise and counterclockwise motions around the nanotube. Due to the anisotropy of orbital magnetic moment [38], the energy levels of electron in a carbon nanotube become sensitive to the direction of a magnetic field, which has been applied into the detection of static magnetic fields [39,40] and electrically driven electron spin resonance [33,34]. Although it has been demonstrated that nuclear magnetic fields may influence electron transport [36] and electron spin resonance [31] in a double quantum dot confined in the GaAs heterostructure, it is not clear how the mechanism can be engineered for nanoscale magnetic resonance spectroscopy.

The goal of the present work is to design a quantum sensor based on a carbon nanotube double quantum dot system that can achieve a sensitivity on the order of 10 $\mathrm{nT}/\sqrt{\mathrm{Hz}}$ for weak oscillating magnetic fields, which is sufficient for achieving nuclear magnetic resonance spectroscopy at the single-molecule level. The key idea, which enables us to achieve such a goal, is continuous electrical driving on a carbon nanotube double quantum dot, which leads to resonant leakage current when the driving Rabi frequency matches the fingerprint frequency of a weak signal (e.g., arising from nuclei), see Figs. 1(b) and 1(c). This in turn allows to obtain the relevant information on the weak signal from the electron transport spectroscopy in Pauli blockade regime [28].

In a static magnetic field $\mathbf{B}$, the Hamiltonian of an electron in the nanotube is given by (for simplicity we set $\hbar = 1$) [33,41]

$$\hat{H}(z) = -\frac{1}{2}\Delta_{\mathrm{SO}}\hat{\tau}_3\mathbf{n}(z)\cdot\hat{\boldsymbol{\sigma}} - \frac{1}{2}\Delta_{KK'}\left(\hat{\tau}_1\cos\varphi + \hat{\tau}_2\sin\varphi\right) + \frac{1}{2}g_s\mu_B\mathbf{B}\cdot\hat{\boldsymbol{\sigma}} + g_{\mathrm{orb}}\mu_B\mathbf{B}\cdot\mathbf{n}(z)\,\hat{\tau}_3, \quad (1)$$

where $\hat{\boldsymbol{\tau}} = (\hat{\tau}_1, \hat{\tau}_2, \hat{\tau}_3)$ and $\hat{\boldsymbol{\sigma}} = (\hat{\sigma}_x, \hat{\sigma}_y, \hat{\sigma}_z)$ are the Pauli operators of valley and spin, $\mathbf{n}(z) = \cos\theta(z)\,\hat{z} + \sin\theta(z)\,\hat{x}$ is the local tangent unit vector with $\theta(z)$ the angle between $\mathbf{n}(z)$ and $\hat{z}$, Δ_{SO} is the spin-orbit coupling strength [42], $\Delta_{KK'}$ and φ are the magnitude and phase of valley mixing [43], g_s and g_{orb} are the g factors of spin and valley, respectively. At $\theta(z_0) = 0$ and $\mathbf{B} = 0$, four eigenstates form two Kramers doublets $\{|\Uparrow^*\rangle, |\Downarrow^*\rangle\}$ and $\{|\Uparrow\rangle, |\Downarrow\rangle\}$, which are separated by an energy gap $\Delta E_0 = \left(\Delta_{\mathrm{SO}}^2 + \Delta_{KK'}^2\right)^{1/2}$. Each doublet can serve as a valley-spin qubit, which shows different energy splittings in the parallel ($\mathbf{B} = B_z\hat{z}$) and perpendicular ($\mathbf{B} = B_x\hat{x}$) magnetic field due to the anisotropic magnetic moment. As mediated by a bent nanotube [44], the qubit can be electrically driven while the quantum dot is driven back and forth with frequency ω and amplitude Δz_m by applying a microwave frequency gate voltage.

The effective Hamiltonian of a driven valley-spin qubit in the magnetic field $\mathbf{B} = \{B_x, 0, B_z\}$ is [41] $\hat{H}_e = \frac{1}{2}\left(\omega_x\hat{s}_x + \omega_z\hat{s}_z\right) + \Omega_x\cos(\omega t)\,\hat{s}_x + \Omega_z\cos(\omega t)\,\hat{s}_z$, where $\hat{s}_{x,y,z}$ are Pauli operators of the valley-spin qubit and $\omega_x = g_\perp\mu_B B_x$, $\omega_z = g_\parallel\mu_B B_z$, with $g_\perp = g_s\sin\zeta$, $g_\parallel = g_s - 2ag_{\mathrm{orb}}\cos\zeta$. The characteristic parameter ζ is defined as $\tan\zeta = \Delta_{KK'}/\Delta_{\mathrm{SO}}$, and a takes the value ±1 for the upper and lower Kramers doublets, respectively. We choose $\omega = \omega_0 \equiv (\omega_x^2 + \omega_z^2)^{1/2}$ and obtain a dressed valley-spin qubit under the conditions $\Omega_x, \Omega_z \ll \omega_0$ as described by (see more details in Appendix A)

$$\hat{H}_d = \frac{1}{2}\Omega_d\hat{S}_x, \quad (2)$$

where $\hat{S}_x$ is the Pauli operator in the eigenbasis of $\hat{H}_0 = (1/2)\left(\omega_x\hat{s}_x + \omega_z\hat{s}_z\right)$ and the driving Rabi frequency is

$\Omega_d = \Omega_x \cos\gamma - \Omega_z \sin\gamma$ with $\tan\gamma = \omega_x/\omega_z$. Note that the effect of fluctuation in the driving fields can be mitigated by concatenated driving schemes [45].

We consider a double quantum dot in the *n-p* region and encode a valley-spin qubit in the lower Kramers doublet for both quantum dots. In the Pauli blockade regime, electron tunneling is forbidden when two electrons in the $(1,1)$ configuration are in a triplet state [46]. The leakage current can be obtained from the quantum-transport master equation (see more details in Appendix B). When the Rabi frequency of an applied continuous driving field on the valley-spin qubits matches the frequency of local signal fields, e.g., from the hyperfine coupling between the left quantum dot and a single molecule, additional electron tunneling channels open up, see Fig. 1(c). In the following, we show that the change in the leakage current through such a nanotube quantum dot system can serve as a highly sensitive probe for selective detection of localized external signals.

III. SENSING OF A WEAK OSCILLATING FIELD

To illustrate the working principle of nanoscale magnetic resonance spectroscopy using a nanotube quantum sensor, we first consider the measurement of an oscillating magnetic field (e.g., arising from a local magnetic moment) $\mathbf{b}(t) = b\cos(\omega_c t)\,\hat{z}$ acting on the left quantum dot, where the right quantum dot is out of the nanoscale field due to the much larger distance from the left quantum dot. The effective Hamiltonian in the $(1,1)$ subspace is

$$\hat{H}_{sB} = \frac{1}{2}\Omega_d \hat{S}_x^{(1)} + \Omega_c \cos(\omega_c t)\,\hat{S}_z^{(1)} + \frac{1}{2}\Omega_d \hat{S}_x^{(2)}, \qquad (3)$$

where $\hat{S}_{x,z}^{(j)}$ are the Pauli operators of the left ($j=1$) and right ($j=2$) dressed valley-spin qubit, and $\Omega_c = g_\parallel \mu_B b/2$ represents the coupling strength of the left dressed valley-spin qubit to the weak oscillating magnetic field. The Hamiltonian in the $(0,2)$ subspace is $H_\Delta = \Delta\,|S_g\rangle\langle S_g|$ with the energy detuning Δ, and the tunneling Hamiltonian is $H_t = J(|S\rangle\langle S_g| + |S_g\rangle\langle S|)$. In the new picture after making a transformation $\hat{S}_x \leftrightarrow \hat{S}_z$ and using rotating-wave approximation, we introduce the basis states including

$$|A_0\rangle = \frac{1}{\sqrt{2}}\begin{pmatrix}\cos\vartheta\\ \sin\vartheta\\ \sin\vartheta\\ -\cos\vartheta\end{pmatrix}, \quad |A_\pm\rangle = \frac{1}{2}\begin{pmatrix}\pm 1+\sin\vartheta\\ -\cos\vartheta\\ -\cos\vartheta\\ \pm 1-\sin\vartheta\end{pmatrix} \qquad (4)$$

and the singlet state $|S\rangle = (1/\sqrt{2})(0\ \ -1\ \ 1\ \ 0)^T$ with $\cos\vartheta = \Omega_c/\lambda$, $\sin\vartheta = 2\delta/\lambda$, $\delta = \Omega_d - \omega_c$ and $\lambda = \left(4\delta^2 + \Omega_c^2\right)^{1/2}$, to rewrite the Hamiltonian $\hat{H}_{sB}$ as

$$\hat{H}''_{sB} = \begin{pmatrix}0 & 0 & 0 & J_S^0\\ 0 & \lambda/2 & 0 & J_S^+\\ 0 & 0 & -\lambda/2 & J_S^-\\ J_S^0 & J_S^+ & J_S^- & 0\end{pmatrix}, \qquad (5)$$

where the local-field-induced tunneling rates are $J_S^0 = -\Omega_c^2/(2\lambda)$ and $J_S^+ = J_S^- = \delta\Omega_c/\left(\sqrt{2}\lambda\right)$ (see more details in Appendix B).

The above Hamiltonian reveals two essential ingredients of the present nanotube quantum sensor. Firstly, in the absence of an oscillating magnetic field, all of the channels to the state $|S\rangle$ are closed, and the leakage current is only contributed by the state $|S\rangle$. The external oscillating field opens up three additional channels $|A_{0,\pm}\rangle \leftrightarrow |S\rangle \leftrightarrow |S_g\rangle$ for electron tunneling, see Fig. 1(c), and thus can significantly influence the leakage current. Secondly, the transition $|A_0\rangle \leftrightarrow |S\rangle$ is most efficient when $\Omega_d = \omega_c$, as shown in Fig. 2(a). In contrast, the transitions $|A_\pm\rangle \leftrightarrow |S\rangle$ play the most significant role with a slight detuning between Ω_d and ω_c, which is verified by the resonant dip of leakage current in Figs. 2(b) and 2(c). As the electron injected from the source is unpolarized, the total leakage current reflects an overall contribution of all tunneling channels. As the system evolves, the transitions $|A_\pm\rangle \leftrightarrow |S\rangle$ becomes dominant, which leads to a pronounced resonant dip as evident in Fig. 2(d). These features demonstrate the feasibility of using such a nanotube quantum sensor to

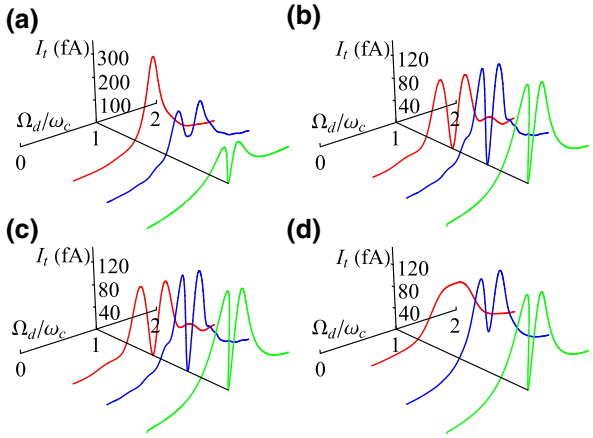

FIG. 2. Illustration of quantum-sensing mechanism. (a)–(d) Leakage current I_t as a function of the driving Rabi frequency Ω_d/ω_c with the initial state $|A_0\rangle$ (a), $|A_+\rangle$ (b), $|A_-\rangle$ (c) and the unpolarized electron spin state (d) in the $(0,1)$ subspace at time $t = 0.5$ μs (red), 1 μs (blue), 10 μs (green), respectively. The parameters are $g_{\rm orb} = 12$, $\Delta_{\rm SO} = 0.8$ meV, $\Delta_{KK'} = 0.2$ meV, $\varphi = 0$ for both electrons [34,41], and $\omega_c = (2\pi)\,5$ MHz, $b = 6$ μT for the oscillating signal field, the electron injection and ejection rate are $\Gamma_L = \Gamma_R = (2\pi)\,8$ MHz and the tunneling rate is $J = (2\pi)\,2$ MHz.

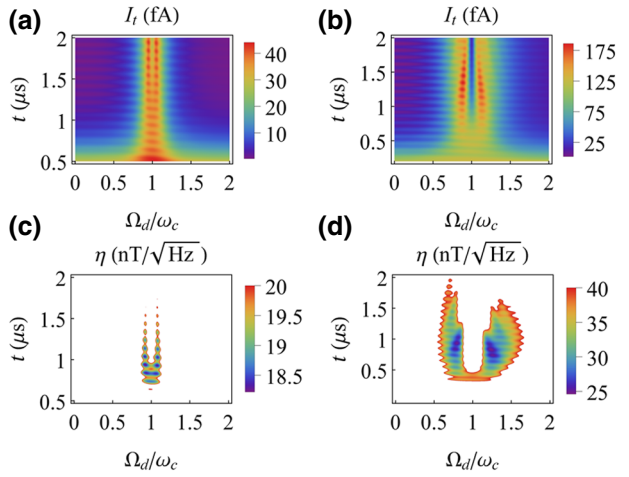

FIG. 3. Performance of measurement sensitivity. (a),(b) Leakage current I_t and (c),(d) estimated sensitivity η (at the resonant peaks and dip of leakage current) as a function of the driving Rabi frequency Ω_d/ω_c and the evolution time t for an oscillating magnetic field with different amplitudes: (a),(c) $b = 2$ μT and (b),(d) $b = 6$ μT. The system starts from one unpolarized electron located in the right quantum dot as the initial state. The other parameters are the same as Fig. 2.

selectively detect a weak oscillating magnetic field from driving-field-induced variations in the leakage current.

By sweeping the Rabi frequency Ω_d of the driving field, a resonance appears in the leakage current when it matches the frequency of the weak oscillating magnetic field emanating from the target (i.e., $\Omega_d = \omega_c$), as shown in Figs. 3(a) and 3(b). Such a resonance measurement offers an efficient way to identify the frequency of the external signal, which provides a basis for single-molecule nuclear magnetic resonance spectroscopy. We further analyze the shot-noise limited sensitivity for the measurement of the amplitude of a weak oscillating field from the instantaneous leakage current I at time t, which is defined by $\eta = \Delta I \sqrt{t}\,(\partial_b I)^{-1}$. We estimate the achievable sensitivity from the measurement of the resonant leakage current in the weak field regime as shown in Figs. 3(c) and 3(d), which implies that the sensitivity can reach the order of 10 nT/$\sqrt{\text{Hz}}$ by measuring the instantaneous leakage current after an evolution time of a few microseconds using the feasible experimental parameters given in Fig. 2.

IV. NANOSCALE MAGNETIC RESONANCE SPECTROSCOPY

Based on the idea presented and analyzed above in the scenario of measuring a weak oscillating signal field, we proceed to demonstrate the applicability of the present scheme for nanoscale magnetic resonance spectroscopy at a single-molecule level. Without loss of generality, we assume that a target molecule is attached on the surface of the nanotube close to the left quantum dot. The interaction strength of magnetic dipole-dipole coupling between the nuclear spins of the target molecule and the valley-spin qubit is $h_n = \mu_0 \mu_B \mu_N g_n g_\parallel / \left(4\pi r^3\right)$, where r represents the distance from the valley-spin qubit and individual nuclear spins. Two unique features of the present proposal are responsible for its excellent performance, namely a large value of $g_\parallel$ (due to a much more prominent orbital g factor, g_{orb}) and the achievable small sensor-target distance r (which benefits from the compact dimension of nanotube).

A single molecule is characterized by different species of nuclear spins with multiple Larmor frequencies. For each nuclear spin, an effective magnetic field introduced by its Larmor precession influences the energy levels of the left quantum dot through the magnetic dipole-dipole coupling. It leads to individual resonance signals of leakage current that are detected by the present driven nanotube quantum sensor. The identification of these characteristic Larmor frequencies, as implemented by sweeping the Rabi frequency of continuous driving, provides a fingerprint for the detection of single molecules. As an example, we consider phosphine (PH_3) and hydrogen fluoride (HF) molecules, both of which are toxic gases. As shown in Fig. 4, owing to the half-integer nuclear spins ^{1}H, ^{19}F, and ^{31}P, the leakage current clearly exhibits resonances when the Rabi frequency of continuous driving matches the condition $\Omega_d = \gamma_n B$, where γ_n is the gyromagnetic ratio corresponding to individual nuclear species. We remark that electron injection (ejection) rates and the tunneling rate can be tuned by local gate voltages in order to optimize the performance of the protocol (see more details in Appendix D).

V. FEASIBILITY OF EXPERIMENTAL REALIZATION

Current experimental advances in fabricating nanotube quantum dots and electrically driven spin resonance quantum control facilitates the implementation of our proposed scheme. The key ingredient for experimental realization is the tuneable Rabi frequency of electric continuous driving Ω_d. The driving Rabi frequency depends on the bending parameter $(\partial_z \theta)_{z=z_0}$ and the oscillation amplitude Δz_m of the quantum dot, the required value of which is feasible with the state-of-the-art experiment capability [34,41]. The scheme prefers two valley-spin qubits that have the same valley mixing $\Delta_{KK'}^{(j)}$ thereby the same characteristic parameter ζ_j for two valley-spin qubits. In order to compensate for nonuniformity in quantum dots and achieve the best sensing performance, we adopt a bent arc shape nanotube with an appropriate tilted angle. By applying a magnetic field in the $\hat{x}$-$\hat{z}$ plane with the proper components of B_x, B_z, we find that two valley-spin qubits can have identical parameters ζ_j (see more details in Appendix B).

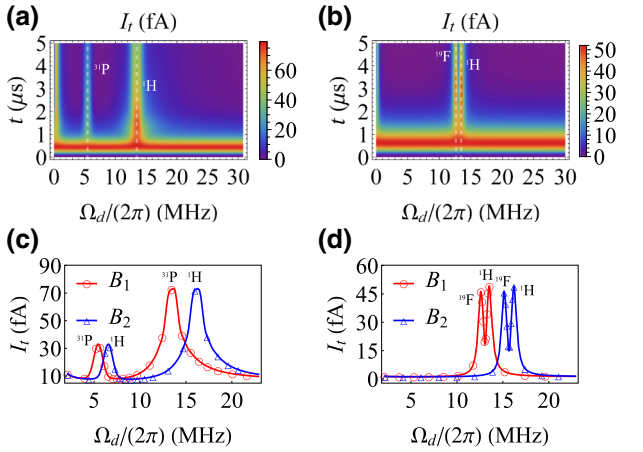

FIG. 4. Single-molecule magnetic resonance spectroscopy. (a),(b) Leakage current I_t as a function of the driving Rabi frequency Ω_d and the evolution time t for the detection of a single PH_3 molecule with $\Gamma_L = (2\pi)\,1$ MHz, $\Gamma_R = (2\pi)\,0.6$ MHz, $J = (2\pi)\,0.55$ MHz (a) and a single HF molecule with $\Gamma_L = (2\pi)\,1$ MHz, $\Gamma_R = (2\pi)\,0.4$ MHz, $J = (2\pi)\,0.35$ MHz (b) in the magnetic field $\mathbf{B} = \{300, 0, 100\}$ mT. The dash lines (white) in (a),(b) represent the corresponding Larmor frequencies. (c),(d) Leakage current I_t as a function of the driving Rabi frequency Ω_d at time $t = 1.5$ μs for the detection of a single PH_3 molecule (c) and at time $t = 3$ μs for the detection of a single HF molecule (d) in different magnetic fields with $\mathbf{B}_1 = \{300, 0, 100\}$ mT and $\mathbf{B}_2 = \{360, 0, 120\}$ mT. The other parameters are the same as Fig. 2.

The main decoherence that may affect the performance of the present carbon nanotube quantum sensor arises from the thermal phonons, the environmental nuclear spins and the charge fluctuation. At low temperature $T = 100$ K, the dominated bending-mode phonon-mediated spin relaxation time is about 1 μs [47], which is much longer than the electron tunneling time in a quantum dot. The influence of nuclei may be mitigated by synthesizing a carbon nanotube with isotopically purified $^{12}CH_4$, allowing for the fabrication of almost nuclei-spin-free devices [23,48,49]. In addition, the driving via continuous control fields serves to suppress noise effects from nuclear impurities in the device, which underlines their importance in our scheme. Our numerical simulation shows that the performance is robust given feasible isotopic engineering (see more details in Appendix C). As the carbon nanotube quantum dot is gate defined, the charge noise modifies the energy levels of the quantum dot, i.e., inducing fluctuations of the energy detuning Δ between the singlet states $|S\rangle$ and $|S_g\rangle$ [40], the role of which in our scheme is mainly the suppression of effective tunneling. The charge noise is slow [50] and its influence can be compensated by optimizing the parameters Γ_L, Γ_R, and J to sustain the leakage current (see more details in Appendix C). We stress that this is quite different from the dephasing effect on the coherence time of the qubit involving the singlet state $|S_g\rangle$ in the (0,2) subspace [34], where the energy splitting of the qubit relies on the energy detuning Δ.

We note that the higher-order tunneling (cotunneling) processes [51,52] may also have an influence on our scheme. As the cotunneling corrections $\propto \Gamma_L\Gamma_R$ [51,53], it is helpful to make the tunnel rates small for the suppression of cotunneling current. In our scheme, the tunnel rates Γ_L, Γ_R are $1 \sim 2$ orders of magnitude smaller than the values in Ref. [52], thus the cotunneling current here is estimated to be much less than 3 fA, which does not significantly influence the performance of our scheme. Overall, we remark that the implementation of our proposal may require new experimental efforts, the feasibility of which appears promising.

VI. CONCLUSIONS & OUTLOOK

To summarize, we propose a new platform for nanoscale magnetic resonance spectroscopy using a continuously driven carbon nanotube double quantum dot as a quantum sensor. The system allows a high sensitivity to be achieved due to its unique features of a large valley g factor and ultra-small dimension. In particular, our simulation demonstrates that such a quantum sensor may identify individual nuclear spin and detect a single molecule. The all-electric control and readout techniques make it appealing for on-chip quantum-sensing device integration. Assisted by the functionalized carbon nanotube [54,55], such a quantum sensor can serve as a nanoscale probe to capture the target molecule selectively and provide a new route to implement nanoscale magnetic resonance spectroscopy at a single-molecule level with a wide range of potential applications both in basic science and applied technology.

ACKNOWLEDGMENTS

We thank Ying Li, Guido Burkard, and Andras Palyi for valuable discussions and suggestions. The work is supported by National Natural Science Foundation of China (Grants No. 11874024, No. 11574103, No. 11690030, and No. 11690032). W.S. is supported by the Postdoctoral Innovation Talent Program, H.L. is also supported by the China Postdoctoral Science Foundation Grant (Grant No. 2016M602274). M.B.P. is supported by the EU projects ASTERIQS and HYPERDIAMOND, the ERC Synergy grant BioQ, and the BMBF via DiaPol and NanoSpin.

APPENDIX A: DERIVATION OF EFFECTIVE HAMILTONIAN

Electrons in a nanotube have two angular-momentum quantum numbers, arising from the spin and the valley degree of freedom. These two degrees of freedom are coupled via spin-orbit interaction [42]. In addition, two valley

states are coupled to each other by electrical disorder and contact electrodes [43]. We introduce the identity and Pauli matrices in the spin space $\hat{\sigma}_i$ with $i = \{0, x, y, z\}$ and the three-dimensional spin vector $\hat{\boldsymbol{\sigma}} \equiv \left\{\hat{\sigma}_x, \hat{\sigma}_y, \hat{\sigma}_z\right\}$. The positive and negative projections of $\hat{\sigma}_z$ (component of $\hat{\sigma}$ along the $\hat{z}$ axis) are denoted by $\{|\uparrow\rangle, |\downarrow\rangle\}$. Similarly, the identity and Pauli matrices in the valley space are denoted as $\hat{\tau}_j$ with $j = \{0, 1, 2, 3\}$ and the three-dimensional valley vector $\hat{\boldsymbol{\tau}} \equiv \left\{\hat{\tau}_1, \hat{\tau}_2, \hat{\tau}_3\right\}$, where we choose $\left\{\left|K'\right\rangle, |K\rangle\right\}$ as the positive and negative projections of $\hat{\tau}_3$ [component of $\hat{\tau}$ along $\mathbf{n}(z) = \cos\theta(z)\,\mathbf{z} + \sin\theta(z)\,\mathbf{x}$, which is a local tangent unit vector of the nanotube with $\theta(z)$ the angle between $\mathbf{n}(z)$ and $\mathbf{z}$]. In a static magnetic field $\mathbf{B}$, the Hamiltonian of an electron can be written as [33,41]

$$\hat{H} = -\frac{1}{2}\Delta_{\mathrm{SO}}\hat{\tau}_3\mathbf{n}(z)\cdot\hat{\boldsymbol{\sigma}} - \frac{1}{2}\Delta_{KK'}\left(\hat{\tau}_1\cos\varphi + \hat{\tau}_2\sin\varphi\right) + \frac{1}{2}g_s\mu_B\mathbf{B}\cdot\hat{\boldsymbol{\sigma}} + g_{\mathrm{orb}}\mu_B\mathbf{B}\cdot\mathbf{n}(z)\,\hat{\tau}_3, \tag{A1}$$

where Δ_{SO} is the spin-orbit coupling strength, $\Delta_{KK'}$ and φ are the magnitude and phase of valley mixing, g_s and g_{orb} are the spin and orbital g factors, respectively. We remark that g_{orb} is much larger than g_s, and provides an advantage for magnetic field sensing [40]. At $\theta(z_0) = 0$ and $\mathbf{B} = 0$, four eigenstates are separated by an energy gap $\Delta E_0 = \left(\Delta_{\mathrm{SO}}^2 + \Delta_{KK'}^2\right)^{1/2}$ and form two Kramers doublets $\{|\Uparrow^*\rangle, |\Downarrow^*\rangle\}$ and $\{|\Uparrow\rangle, |\Downarrow\rangle\}$ with

$$\left|\Uparrow^*\right\rangle = -\cos(\zeta/2)\left|K'\right\rangle|\downarrow\rangle + \sin(\zeta/2)\,|K\rangle\,|\downarrow\rangle, \tag{A2}$$

$$\left|\Downarrow^*\right\rangle = -\sin(\zeta/2)\left|K'\right\rangle|\uparrow\rangle + \cos(\zeta/2)\,|K\rangle\,|\uparrow\rangle, \tag{A3}$$

$$|\Uparrow\rangle = \cos(\zeta/2)\left|K'\right\rangle|\uparrow\rangle + \sin(\zeta/2)\,|K\rangle\,|\uparrow\rangle, \tag{A4}$$

$$|\Downarrow\rangle = \sin(\zeta/2)\left|K'\right\rangle|\downarrow\rangle + \cos(\zeta/2)\,|K\rangle\,|\downarrow\rangle, \tag{A5}$$

with $\tan\zeta = \Delta_{KK'}/\Delta_{\mathrm{SO}}$ (without loss of generality we consider $\varphi = 0$), either of which can serve as a valley-spin qubit.

Electrons in a nanotube can be longitudinally confined to form a quantum dot by introducing tunnel barriers, which can be created by modifying the electrostatic potential with gate voltages. For a double quantum dot, even the tunneling of a single electron is permitted by Coulomb blockade, the transition from a ground $(1,1)$-triplet state with one electron in each dot to a ground $(0,2)$-singlet state with both electrons in the right dot is blocked by the Pauli exclusion principle, hence the leakage current is zero. In a carbon nanotube, the energy difference between an excited $(0,2)$-triplet state and a ground $(0,2)$-singlet state can be one or two orders of magnitude smaller than in III–V materials, which gives rise to the transition from a ground $(1,1)$-triplet state to an excited $(0,2)$-triplet state, hence the Pauli blockade does not work perfectly. A robust Pauli blockade in a carbon nanotube is most evident with a double quantum dot tuned into the *n-p* region, where the first shells of electrons and holes are separated by a large gap [28].

Based on the Pauli blockade in a double quantum dot, we consider two valley-spin qubits both of which are encoded in the lower Kramers doublet $\{|\Uparrow\rangle, |\Downarrow\rangle\}$, then the leakage current can be regarded as a *meter* of the right valley-spin qubit and the left valley-spin qubit servers as a quantum *probe* interacting with a target. In our scheme, two dressed valley-spin qubits in a double quantum dot can be used as a nanotube quantum sensor to detect, e.g., a local magnetic field or a locally interacting spin.

1. Dressed valley-spin qubit

A valley-spin qubit in a static magnetic field $\mathbf{B}$ can be electrically driven when the quantum dot in a bent nanotube is driven by a microwave gate voltage [33,34]. We denote the frequency and the amplitude of the driven motion of the quantum dot as ω and Δz_m. The effective Hamiltonian of such a driven valley-spin qubit can be written as follows [41]:

$$\hat{H}_e = \frac{1}{2}\mathbf{g}^*\mu_B\cdot\mathbf{B}\cdot\hat{\mathbf{s}} + \Omega_x\cos(\omega t)\,\hat{s}_x + \Omega_z\cos(\omega t)\,\hat{s}_z, \tag{A6}$$

where $\mathbf{s}\hat{=}\left\{\hat{s}_x, \hat{s}_y, \hat{s}_z\right\}$ is the Pauli operator of a valley-spin qubit in the basis of the lower Kramers doublet $\{|\Uparrow\rangle, |\Downarrow\rangle\}$ with

$$|\Uparrow\rangle = \cos(\zeta/2)\left|K'\right\rangle|\uparrow\rangle + \sin(\zeta/2)\,|K\rangle\,|\uparrow\rangle, \tag{A7}$$

$$|\Downarrow\rangle = \sin(\zeta/2)\left|K'\right\rangle|\downarrow\rangle + \cos(\zeta/2)\,|K\rangle\,|\downarrow\rangle. \tag{A8}$$

The effective g tensor is

$$\mathbf{g}^* = \begin{pmatrix} g_\perp & 0 & 0 \\ 0 & g_\perp & 0 \\ 0 & 0 & g_\parallel, \end{pmatrix} \tag{A9}$$

with $g_\perp = g_s\sin\zeta$, $g_\parallel = g_s + 2g_{\mathrm{orb}}\cos\zeta$. The effective driving Rabi frequencies are

$$\Omega_x = \sin(2\zeta)\,g_{\mathrm{orb}}\mu_B B_z\delta_\theta/2, \tag{A10}$$

$$\Omega_z = \left(2g_{\mathrm{orb}}\cos\zeta + g_s\cos^2\zeta\right)\mu_B B_x\delta_\theta/2, \tag{A11}$$

with $\delta_\theta = (\partial_z\theta)_{z=z_0}\,\Delta z_m$. Considering a magnetic field $\mathbf{B} = \{B_x, 0, B_z\}$ in the x-z plane, the effective Hamiltonian

can be written as

$$\hat{H}_e = \frac{1}{2}\left(\omega_x \hat{s}_x + \omega_z \hat{s}_z\right) + \Omega_x \cos(\omega t)\,\hat{s}_x + \Omega_z \cos(\omega t)\,\hat{s}_z, \tag{A12}$$

where

$$\omega_x = g_\perp \mu_B B_x, \tag{A13}$$

$$\omega_z = g_\parallel \mu_B B_z. \tag{A14}$$

The eigenvalues of $\hat{H}_0 = \frac{1}{2}\left(\omega_x \hat{s}_x + \omega_z \hat{s}_z\right)$ are

$$\epsilon_{1,2} = \pm\sqrt{\omega_x^2 + \omega_z^2}/2, \tag{A15}$$

and the corresponding eigenstates are

$$|\psi_1\rangle = \cos(\gamma/2)\,|\Uparrow\rangle + \sin(\gamma/2)\,|\Downarrow\rangle\,, \tag{A16}$$

$$|\psi_2\rangle = -\sin(\gamma/2)\,|\Uparrow\rangle + \cos(\gamma/2)\,|\Downarrow\rangle\,, \tag{A17}$$

with

$$\cos\gamma = \omega_z/\sqrt{\omega_x^2 + \omega_z^2}, \tag{A18}$$

$$\sin\gamma = \omega_x/\sqrt{\omega_x^2 + \omega_z^2}. \tag{A19}$$

We can rewrite the Hamiltonian $\hat{H}_e$ in the basis of $\{|\psi_1\rangle, |\psi_2\rangle\}$ as follows:

$$\hat{H}_e' = \frac{1}{2}\omega_0 \hat{S}_z + g_z \cos(\omega t)\,\hat{S}_z + g_x \cos(\omega t)\,\hat{S}_x, \tag{A20}$$

with

$$\omega_0 = \sqrt{\omega_x^2 + \omega_z^2}, \tag{A21}$$

$$g_z = \Omega_z \cos\gamma + \Omega_x \sin\gamma, \tag{A22}$$

$$g_x = \Omega_x \cos\gamma - \Omega_z \sin\gamma, \tag{A23}$$

where $\hat{S}_z$ and $\hat{S}_x$ are Pauli matrices in the basis of $|\psi_1\rangle$ and $|\psi_2\rangle$. We choose $\omega = \omega_0$ and use rotating-wave approximation under the conditions $g_x, g_z \ll \omega_0$, which leads to a dressed valley-spin qubit system with the following effective Hamiltonian:

$$\hat{H}_d = \frac{1}{2} g_x \hat{S}_x. \tag{A24}$$

2. Coupling between a dressed valley-spin qubit and a local oscillating signal field

We first consider the situation in which a driven valley-spin qubit is coupled to a weak oscillating signal field $\mathbf{b} = b\cos(\omega_c t)\,\mathbf{z}$ in addition to the static magnetic field $\mathbf{B} = \{B_x, 0, B_z\}$ with $|\mathbf{b}| \ll |\mathbf{B}|$. According to Eqs. (A6)–(A12), the total Hamiltonian can be written as

$$\hat{H}_{eB} = \frac{1}{2}\left(\omega_x \hat{s}_x + \omega_z \hat{s}_z\right) + \Omega_x \cos(\omega t)\,\hat{s}_x + \Omega_z \cos(\omega t)\,\hat{s}_z + \Omega_c \cos(\omega_c t)\,\hat{s}_z, \tag{A25}$$

with $\Omega_c = g_\parallel \mu_B b/2$, where $\mathbf{b}$ only contributes to the first-order perturbative approximation of $\hat{H}$ [Eq. (A1)]. The above Hamiltonian $\hat{H}_{eB}$ can be written in the eigenbases of $\hat{H}_0 = \frac{1}{2}\left(\omega_x \hat{s}_x + \omega_z \hat{s}_z\right)$ as follows:

$$\hat{H}_{eB}' = \frac{1}{2}\omega_0 \hat{S}_z + g_z \cos(\omega t)\,\hat{S}_z + g_x \cos(\omega t)\,\hat{S}_x + \Omega_c \cos\gamma \cos(\omega_c t)\,\hat{S}_z - \Omega_c \sin\gamma \cos(\omega_c t)\,\hat{S}_x. \tag{A26}$$

By choosing $\omega = \omega_0$ and using rotating-wave approximation under the conditions $\Omega_c \ll \omega_c, g_x, g_z \ll \omega_0$, we can obtain the following effective Hamiltonian for a dressed valley-spin qubit coupled to an oscillating magnetic field as

$$\hat{H}_{dB} = \frac{1}{2} g_x \hat{S}_x + \Omega_c \cos(\omega_c t)\,\hat{S}_z, \tag{A27}$$

where we assume $\cos\gamma \approx 1$ that is valid when $\omega_x \ll \omega_z$.

3. Coupling between a dressed valley-spin qubit and a nuclear spin

We proceed to consider the situation in which a driven valley-spin qubit is coupled to a nuclear spin via magnetic dipole-dipole interaction. The interaction strength is usually much weaker than the static magnetic field $\mathbf{B} = \{B_x, 0, B_z\}$. The Hamiltonian of the total system is

$$\hat{H}_{en} = \frac{1}{2}\left(\omega_x \hat{s}_x + \omega_z \hat{s}_z\right) + \Omega_x \cos(\omega t)\,\hat{s}_x + \Omega_z \cos(\omega t)\,\hat{s}_z + g_n \mu_N \mathbf{B}\cdot\hat{\mathbf{I}} + \left(\frac{\mu_0 \mu_B \mu_N}{4\pi r^3}\right)\left\{\left(\mathbf{g}^*\cdot\hat{\mathbf{s}}/2\right)\cdot\left(g_n\hat{\mathbf{I}}\right) - 3\left[\left(\mathbf{g}^*\cdot\hat{\mathbf{s}}/2\right)\cdot\mathbf{n_r}\right]\left[\left(g_n\hat{\mathbf{I}}\right)\cdot\mathbf{n_r}\right]\right\}, \tag{A28}$$

where g_n is the g factor of the nuclear spin, $\mathbf{I} \hat{=} \left\{\hat{I}_x, \hat{I}_y, \hat{I}_z\right\}$ is the spin operator of the nuclear spin and $\mathbf{r} = r\mathbf{n_r}$ is the vector connecting the valley-spin qubit and the nuclear spin with a distance r and a unit vector $\mathbf{n_r} = \left\{n_x, n_y, n_z\right\}$.

Written in the eigenbases of $\hat{H}_0$, one can obtain

$$\begin{aligned}\hat{H}'_{en} = &\frac{1}{2}\omega_0\hat{S}_z + g_z\cos(\omega t)\,\hat{S}_z + g_x\cos(\omega t)\,\hat{S}_x \\ &+ g_n\mu_N\mathbf{B}\cdot\hat{\mathbf{I}} + \left(\frac{\mu_0\mu_B\mu_N g_n}{8\pi r^3}\right) \\ &\times\left\{\left[g_\perp\left(\sin\gamma\hat{S}_z + \cos\gamma\hat{S}_x\right)\hat{I}_x\right.\right. \\ &+g_\perp\hat{S}_y\hat{I}_y + g_\parallel\left(\cos\gamma\hat{S}_z - \sin\gamma\hat{S}_x\right)\hat{I}_z\Big] \\ &- 3\left[g_\perp n_x\left(\sin\gamma\hat{S}_z + \cos\gamma\hat{S}_x\right) + g_\perp n_y\hat{S}_y\right. \\ &\left.\left.+g_\parallel n_z\left(\cos\gamma\hat{S}_z - \sin\gamma\hat{S}_x\right)\right]\left(n_x\hat{I}_x + n_y\hat{I}_y + n_z\hat{I}_z\right)\right\}. \end{aligned} \tag{A29}$$

Similarly, we choose $\omega = \omega_0$ and use rotating-wave approximation under the conditions $g_x, g_z \ll \omega_0$ and $(\mu_0\mu_B\mu_N g_n)/\left(8\pi r^3\right) \ll \omega_0 - (g_n\mu_N|\mathbf{B}|)$, and thereby obtain the following effective Hamiltonian for a dressed valley-spin qubit coupled with a nuclear spin as described by

$$\begin{aligned}\hat{H}_{\rm dn} = &\frac{1}{2}g_x\hat{S}_x + g_n\mu_N\mathbf{B}\cdot\hat{\mathbf{I}} + \frac{h_n}{2}\left[\hat{S}_z\hat{I}_z\right. \\ &\left.-3n_z\hat{S}_z\left(n_x\hat{I}_x + n_y\hat{I}_y + n_z\hat{I}_z\right)\right], \end{aligned} \tag{A30}$$

with $h_n = \mu_0\mu_B\mu_N g_n g_\parallel/\left(4\pi r^3\right)$, where we assume $\omega_x \ll \omega_z$ and thus $\cos\gamma \approx 1$. We remark that the above Hamiltonian can be straightforwardly generalized to the scenario of multiple nuclear spins.

APPENDIX B: DETAILED MECHANISM OF A NANOTUBE QUANTUM SENSOR

To illustrate the basic idea, here we present further details on the sensing mechanism for the detection of a weak oscillating magnetic field using a nanotube quantum sensor. The system dynamics is governed by the following quantum-transport master equation as [56,57]

$$\dot{\rho}_t = -i\left[\hat{\mathcal{H}}, \rho_t\right] + \mathcal{L}\rho_t, \tag{B1}$$

with

$$\hat{\mathcal{H}} = \begin{pmatrix}\hat{\mathcal{H}}_{\rm I} & 0\\ 0 & \hat{\mathcal{H}}_{\rm II}\end{pmatrix}, \tag{B2}$$

where $\hat{\mathcal{H}}_{\rm I}$ and $\hat{\mathcal{H}}_{\rm II}$ correspond to the $(0,1)$ and $(1,1)\oplus(0,2)$ subspaces, respectively, namely

$$\hat{\mathcal{H}}_{\rm I} = \frac{1}{2}\Omega_d\hat{S}_x^{(2)}, \tag{B3}$$

and

$$\begin{aligned}\hat{\mathcal{H}}_{\rm II} = &\frac{1}{2}\Omega_d\hat{S}_x^{(1)} + \Omega_c\cos(\omega_c t)\,\hat{S}_z^{(1)} + \frac{1}{2}\Omega_d\hat{S}_x^{(2)} \\ &+\Delta\left|S_g\right\rangle\left\langle S_g\right| + J\left(|S\rangle\left\langle S_g\right| + \left|S_g\right\rangle\langle S|\right), \end{aligned} \tag{B4}$$

where $|S\rangle$ and $\left|S_g\right\rangle$ are the singlet states in $(1,1)$ and $(0,2)$ subspaces, respectively. We note that $H_t = J\left(|S\rangle\left\langle S_g\right| + \left|S_g\right\rangle\langle S|\right)$ represents the tunneling between two quantum dots, and $H_\Delta = \Delta\left|S_g\right\rangle\left\langle S_g\right|$ is the Hamiltonian in the $(0,2)$ subspace. The superoperator $\mathcal{L}$ is generated by Lindblad operators $L_1 = \sqrt{\Gamma_L}\hat{a}_{1\psi}^\dagger$ and $L_2 = \sqrt{\Gamma_R}\hat{a}_{2\psi}$ describing the processes, by which an unpolarized electron is injected from the source at a rate Γ_L and is ejected to the drain at a rate Γ_R, where ψ denotes a set of complete and orthogonal basis states of a valley-spin qubit. The leakage current at time t can be calculated as follows:

$$I(t) = (e\Gamma_R)\sum_\psi {\rm Tr}\left(\hat{a}_{2\psi}^\dagger\hat{a}_{2\psi}\rho_t\right). \tag{B5}$$

On the other hand, we derive the shot noise of the leakage current [see Eq. (B5)] as follows:

$$\begin{aligned}\Delta I^2 = (e\Gamma_R)^2\sum_\psi\Big\{&{\rm Tr}\left[\left(\hat{a}_{2\psi}^\dagger\hat{a}_{2\psi}\right)^2\rho_t\right] \\ &-\left[{\rm Tr}\left(\hat{a}_{2\psi}^\dagger\hat{a}_{2\psi}\rho_t\right)\right]^2\Big\}. \end{aligned} \tag{B6}$$

Therefore, the shot-noise-limited measurement sensitivity for an evolution time t is given by

$$\eta = \Delta I\sqrt{t}/\left(\frac{\partial I}{\partial b}\right). \tag{B7}$$

1. Tunneling channels for leakage current

The system of a carbon nanotube double quantum dot in the $(1,1)$ charge configuration can be described by the following Hamiltonian:

$$\hat{H}_{sB} = \frac{1}{2}\Omega_d\hat{S}_x^{(1)} + \Omega_c\cos(\omega_c t)\,\hat{S}_z^{(1)} + \frac{1}{2}\Omega_d\hat{S}_x^{(2)}, \tag{B8}$$

where $g_x^{(1)} = g_x^{(2)} \equiv \Omega_d$ and $\hat{S}_{x,z}^{(j)}$ represent the Pauli operators of the left ($j=1$) and right ($j=2$) dressed valley-spin qubits. Here, we assume that both dressed valley-spin qubits are identical. We remark that two dressed valley-spin qubits may not be completely identical due to, e.g., local disorder. We address this issue in detail in the next section. Using rotating-wave approximation under the conditions $\Omega_c \ll \omega_c, \Omega_d$, in the interaction picture with respect

to $\hat{H}_{sB}^{(0)} = (\omega_c/2)\left[\hat{S}_x^{(1)} + \hat{S}_x^{(2)}\right]$, the Hamiltonian $\hat{H}_{sB}$ can be simplified into

$$\hat{H}'_{sB} = \frac{1}{2}\delta\hat{S}_z^{(1)} - \frac{1}{2}\Omega_c\hat{S}_x^{(1)} + \frac{1}{2}\delta\hat{S}_z^{(2)}, \tag{B9}$$

with $\delta = \Omega_d - \omega_c$, where we adopt a transformation $\hat{S}_x \leftrightarrow \hat{S}_z$ for simplicity and use rotating-wave approximation. In the basis of $\{|A_0\rangle, |A_+\rangle, |A_-\rangle, |S\rangle\}$, one can partially diagonalize the Hamiltonian $\hat{H}'_{sB}$ into the following form:

$$\hat{H}''_{sB} = \begin{pmatrix} 0 & 0 & 0 & J_S^0 \\ 0 & \lambda/2 & 0 & J_S^+ \\ 0 & 0 & -\lambda/2 & J_S^- \\ J_S^0 & J_S^+ & J_S^- & 0 \end{pmatrix}, \tag{B10}$$

with $\lambda = \sqrt{4\delta^2 + \Omega_c^2}$, $J_S^0 = -\Omega_c^2/(2\lambda)$, $J_S^{\pm} = \delta\Omega_c/\left(\sqrt{2}\lambda\right)$, where

$$|A_0\rangle = \frac{1}{\sqrt{2}}\begin{pmatrix} \cos\vartheta \\ \sin\vartheta \\ \sin\vartheta \\ -\cos\vartheta \end{pmatrix}, \quad |A_\pm\rangle = \frac{1}{2}\begin{pmatrix} \pm 1 + \sin\vartheta \\ -\cos\vartheta \\ -\cos\vartheta \\ \pm 1 - \sin\vartheta \end{pmatrix}, \tag{B11}$$

with $\cos\vartheta = \Omega_c/\lambda$, $\sin\vartheta = 2\delta/\lambda$, and $|S\rangle = \left(1/\sqrt{2}\right)(0\ -1\ 1\ 0)^T$ is the singlet state, which is the only unblocked state allowing electron tunneling to the $(0,2)$-singlet state $|S_g\rangle$. The other three states $|A_0, \pm\rangle$ are blocked, nevertheless they couple with the singlet state $|S\rangle$, which may open three tunneling channels for leakage current. The transitions $|A_{0,\pm}\rangle \leftrightarrow |S\rangle$ are characterized by the following reduced effective Hamiltonian:

$$\hat{H}_{A_0} = \begin{pmatrix} 0 & -\Omega_c^2/(2\lambda) \\ -\Omega_c^2/(2\lambda) & 0 \end{pmatrix}, \tag{B12}$$

$$\hat{H}_{A_\pm} = \begin{pmatrix} \pm\lambda/2 & \delta\Omega_c/\left(\sqrt{2}\lambda\right) \\ \delta\Omega_c/\left(\sqrt{2}\lambda\right) & 0 \end{pmatrix}, \tag{B13}$$

respectively. In the absence of a weak oscillating magnetic field (namely $\Omega_c = 0$), all of the channels to the state $|S\rangle$ are closed. In this case, the $|S\rangle$ state fraction leads to electron tunneling and a prominent leakage current, see Fig. 5(b). The other three states are blocked, which results in exponentially decay of leakage current. The presence of the weak oscillating field opens three tunneling channels via the transitions $|A_{0,\pm}\rangle \leftrightarrow |S\rangle$. To qualitatively understand the role of frequency detuning δ in these tunneling channels, we assume that two electrons are initialized in the state $|A_{0,\pm}\rangle$, respectively. One can obtain that the average population of the singlet state $|S\rangle$ is

$$P_S^{(0)} = \frac{1}{2}, \tag{B14}$$

$$P_S^{(\pm)} = \frac{4\delta^2\Omega_c^2}{\left(4\delta^2 + \Omega_c^2\right)^2 + 8\delta^2\Omega_c^2}. \tag{B15}$$

For the transition $|A_0\rangle \leftrightarrow |S\rangle$, these two states $|S\rangle$ and $|A_0\rangle$ are on resonance, therefore the transition rate $\Omega_c^2/(2\lambda)$ is maximized when $\delta = 0$. In contrast, the transitions $|A_\pm\rangle \leftrightarrow |S\rangle$ rely on a nonzero frequency detuning, otherwise the transition rate $\delta\Omega_c/\left(\sqrt{2}\lambda\right)$ is instead zero. Thus, these two tunneling channels make the most significant contribution to leakage current with an appropriate nonzero frequency detuning. This is evident by two symmetric peaks in the average singlet-state population when the initial states are $|A_\pm\rangle$, as shown in Fig. 5(a). It can also be seen from Fig. 5(b) that a small frequency detuning can sustain a relatively large leakage current in the steady state.

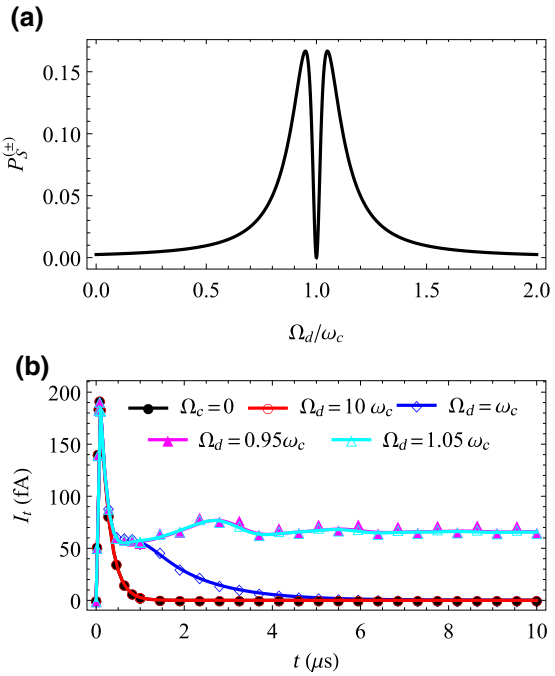

FIG. 5. (a) Average population of the singlet state $|S\rangle$ in the steady state as a function of the driving Rabi frequency Ω_d/ω_c. $P_S^{(\pm)}$ correspond to the initial state $|A_\pm\rangle$, respectively. (b) Leakage current I_t as a function of the evolution time t in the following situations: $\Omega_c = 0$ (no oscillating magnetic field), $\Omega_d = 10\omega_c$ (far detuning), $\Omega_d = \omega_c$ (on resonance), $\Omega_d = 0.95\omega_c$ and $\Omega_d = 1.05\omega_c$ (near resonance), with one unpolarized electron located in the right quantum dot as the initial state. The other parameters are $\omega_c = (2\pi)\,5$ MHz, $\Omega_c = (2\pi)\,0.5$ MHz, $\Gamma_L = \Gamma_R = (2\pi)\,8$ MHz, and $J = (2\pi)\,2$ MHz.

2. Compensation of nonuniformity between two nanotube quantum dots

As the intervalley scattering is induced by electric disorder, it is usually hard to fabricate two valley-spin qubits that have uniform parameters. To be more specific, two nanotube quantum dots may have different valley-mixing parameters $\Delta_{KK'}^{(j)}$ [see Eqs. (A1) and (A6)], which results in different values of the characteristic parameter ζ_j for two valley-spin qubits [see Eqs. (A2)–(A5)]. In order to compensate such a nonuniformity, we consider a bent arc shape nanotube with an tilted angle α, as shown in Fig. 6. When applying a magnetic field in the x-z plane, the magnetic fields for both electrons in the left ($j = 1$) and right ($j = 2$) nanotube quantum dot written in their local coordinates x_j-z_j are

$$B_{x_j}^{(j)} = B_x \cos\alpha + (-1)^{j+1} B_z \sin\alpha, \tag{B16}$$

$$B_{z_j}^{(j)} = B_z \cos\alpha - (-1)^{j+1} B_x \sin\alpha. \tag{B17}$$

The effective Hamiltonian of the driven valley-spin qubit in the left nanotube quantum dot, which interacts with an oscillating magnetic field, as written in its local coordinates x_1-z_1 is

$$\hat{H}_{eB}^{(1)} = \frac{1}{2}\left(\omega_{x_1}^{(1)}\hat{s}_{x_1}^{(1)} + \omega_{z_1}^{(1)}\hat{s}_{z_1}^{(1)}\right) + \Omega_{x_1}^{(1)}\cos(\omega t)\,\hat{s}_{x_1}^{(1)} + \Omega_{z_1}^{(1)}\cos(\omega t)\,\hat{s}_{z_1}^{(1)} + \Omega_c\cos(\omega_c t)\,\hat{s}_{z_1}^{(1)}, \tag{B18}$$

where $\delta_\theta^{(1)} = \left(\partial_{z_1}\theta_1\right)_{z_1=z_0}\Delta z_m^{(1)}$, $\omega_{x_1}^{(1)}$, $\omega_{z_1}^{(1)}$, $\Omega_{x_1}^{(1)}$, $\Omega_{z_1}^{(1)}$ are defined as in Sec. Appendix A.1, in which the parameter ζ_1 is given by $\tan\zeta_1 = \Delta_{KK'}^{(1)}/\Delta_{\mathrm{SO}}^{(1)}$. The Pauli operators of the left valley-spin qubit $\hat{s}_{x_1}^{(1)}, \hat{s}_{y_1}^{(1)}, \hat{s}_{z_1}^{(1)}$ are defined in the following basis:

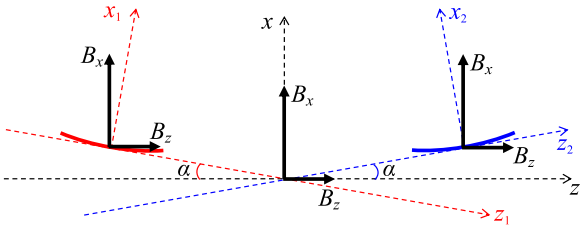

FIG. 6. Schematic diagram of coordinates for two quantum dots in a bent arc shape nanotube with a tilted angle α. Local coordinates x_1-z_1 and coordinates x_2-z_2 are used to describe the Hamiltonian of electron in the left and right quantum dot, respectively. The magnetic field $\mathbf{B} = B_x\mathbf{x} + B_z\mathbf{z}$ is applied in the x-z plane.

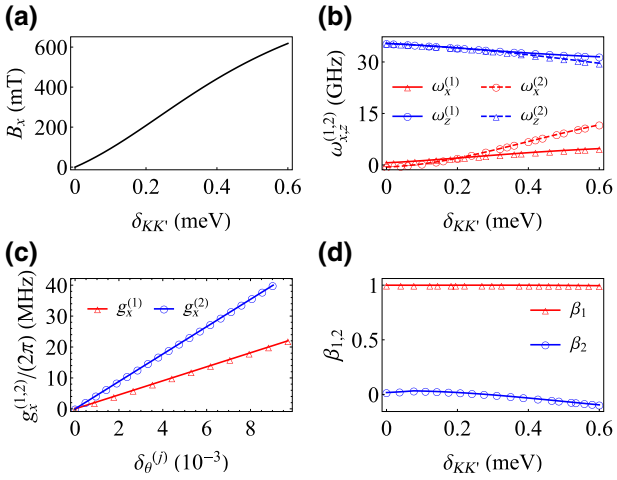

FIG. 7. The parameters to achieve the condition $\omega_0^{(1)} = \omega_0^{(2)}$ and $g_x^{(1)} = g_x^{(2)}$. (a) B_x as a function of the intervalley scattering difference $\delta_{KK'} = \Delta_{KK'}^{(2)} - \Delta_{KK'}^{(1)}$. (b) $\omega_{x,z}^{(1,2)}$ as a function of the intervalley scattering difference $\delta_{KK'}$. (c) For a certain value of $\delta_{KK'} = 0.2$ meV, $g_x^{(1,2)}$ as a function of the driving parameter $\delta_\theta^{(j)}$. (d) $\beta_{1,2}$ as a function of the intervalley scattering difference $\delta_{KK'}$. The other parameters are: $\Delta_{KK'}^{(1)} = 0.2$ meV, $\alpha = 1^\circ$, $B_z = 100$ mT.

$$\left|\Uparrow_1^{(1)}\right\rangle = \cos(\zeta_1/2)\left|K'\right\rangle|\uparrow\rangle + \sin(\zeta_1/2)\,|K\rangle\,|\uparrow\rangle\,, \tag{B19}$$

$$\left|\Downarrow_1^{(1)}\right\rangle = \sin(\zeta_1/2)\left|K'\right\rangle|\downarrow\rangle + \cos(\zeta_1/2)\,|K\rangle\,|\downarrow\rangle\,. \tag{B20}$$

Similarly, the effective Hamiltonian for the driven valley-spin qubit in the right nanotube quantum dot as written in its local coordinates x_2-z_2 is

$$\hat{H}_e^{(2)} = \frac{1}{2}\left(\omega_{x_2}^{(2)}\hat{s}_{x_2}^{(2)} + \omega_{z_2}^{(2)}\hat{s}_{z_2}^{(2)}\right) + \Omega_{x_2}^{(2)}\cos(\omega t)\,\hat{s}_{x_2}^{(2)} + \Omega_{z_2}^{(2)}\cos(\omega t)\,\hat{s}_{z_2}^{(2)} \tag{B21}$$

The corresponding Pauli operators $\hat{s}_{x_2}^{(2)}, \hat{s}_{y_2}^{(2)}, \hat{s}_{z_2}^{(2)}$ are written in the following basis:

$$\left|\Uparrow_2^{(2)}\right\rangle = \cos(\zeta_2/2)\left|K'\right\rangle|\uparrow\rangle + \sin(\zeta_2/2)\,|K\rangle\,|\uparrow\rangle\,, \tag{B22}$$

$$\left|\Downarrow_2^{(2)}\right\rangle = \sin(\zeta_2/2)\left|K'\right\rangle|\downarrow\rangle + \cos(\zeta_2/2)\,|K\rangle\,|\downarrow\rangle\,, \tag{B23}$$

with the characteristic parameter ζ_2 as defined by $\tan\zeta_2 = \Delta_{KK'}^{(2)}/\Delta_{\mathrm{SO}}^{(2)}$.

Therefore, the total effective Hamiltonian in the common coordinates x-z is

$$\begin{aligned}\hat{H}_{\rm tb} &= \exp\left[-i\alpha\hat{s}_{y_1}^{(1)}/2\right]\hat{H}_{eB}^{(1)}\exp\left[i\alpha\hat{s}_{y_1}^{(1)}/2\right]\\ &\quad+\exp\left[i\alpha\hat{s}_{y_2}^{(2)}/2\right]\hat{H}_{e}^{(2)}\exp\left[-i\alpha\hat{s}_{y_2}^{(2)}/2\right]\\ &=\left[\cos\left(\frac{\alpha}{2}\right)-i\hat{s}_{y_1}^{(1)}\sin\left(\frac{\alpha}{2}\right)\right]\hat{H}_{eB}^{(1)}\\ &\quad\times\left[\cos\left(\frac{\alpha}{2}\right)+i\hat{s}_{y_1}^{(1)}\sin\left(\frac{\alpha}{2}\right)\right]\\ &\quad+\left[\cos\left(\frac{\alpha}{2}\right)+i\hat{s}_{y_2}^{(2)}\sin\left(\frac{\alpha}{2}\right)\right]\hat{H}_{e}^{(2)}\\ &\quad\times\left[\cos\left(\frac{\alpha}{2}\right)-i\hat{s}_{y_2}^{(2)}\sin\left(\frac{\alpha}{2}\right)\right]\\ &=\cos^2\left(\frac{\alpha}{2}\right)\hat{H}_{eB}^{(1)}-i\sin\left(\frac{\alpha}{2}\right)\cos\left(\frac{\alpha}{2}\right)\hat{s}_{y_1}^{(1)}\hat{H}_{eB}^{(1)}\\ &\quad+i\sin\left(\frac{\alpha}{2}\right)\cos\left(\frac{\alpha}{2}\right)\hat{H}_{eB}^{(1)}\hat{s}_{y_1}^{(1)}+\sin^2\left(\frac{\alpha}{2}\right)\hat{s}_{y_1}^{(1)}\hat{H}_{eB}^{(1)}\hat{s}_{y_1}^{(1)}\\ &\quad+\cos^2\left(\frac{\alpha}{2}\right)\hat{H}_{e}^{(2)}+i\sin\left(\frac{\alpha}{2}\right)\cos\left(\frac{\alpha}{2}\right)\hat{s}_{y_2}^{(2)}\hat{H}_{e}^{(2)}\\ &\quad-i\sin\left(\frac{\alpha}{2}\right)\cos\left(\frac{\alpha}{2}\right)\hat{H}_{e}^{(2)}\hat{s}_{y_2}^{(2)}+\sin^2\left(\frac{\alpha}{2}\right)\hat{s}_{y_2}^{(2)}\hat{H}_{e}^{(2)}\hat{s}_{y_2}^{(2)}\\ &=\frac{1}{2}\left(\omega_x^{(1)}\hat{s}_x^{(1)}+\omega_z^{(1)}\hat{s}_z^{(1)}\right)\\ &\quad+\Omega_x^{(1)}\cos(\omega t)\,\hat{s}_x^{(1)}+\Omega_z^{(1)}\cos(\omega t)\,\hat{s}_z^{(1)}\\ &\quad+\Omega_c\sin\alpha\cos(\omega_c t)\,\hat{s}_x^{(1)}+\Omega_c\cos\alpha\cos(\omega_c t)\,\hat{s}_z^{(1)}\\ &\quad+\frac{1}{2}\left(\omega_x^{(2)}\hat{s}_x^{(2)}+\omega_z^{(2)}\hat{s}_z^{(2)}\right)+\Omega_x^{(2)}\cos(\omega t)\,\hat{s}_x^{(2)}\\ &\quad+\Omega_z^{(2)}\cos(\omega t)\,\hat{s}_z^{(2)},\end{aligned}\tag{B24}$$

with

$$\omega_x^{(1)}=\omega_{x_1}^{(1)}\cos\alpha+\omega_{z_1}^{(1)}\sin\alpha,\tag{B25}$$

$$\omega_z^{(1)}=\omega_{z_1}^{(1)}\cos\alpha-\omega_{x_1}^{(1)}\sin\alpha,\tag{B26}$$

$$\Omega_x^{(1)}=\Omega_{x_1}^{(1)}\cos\alpha+\Omega_{z_1}^{(1)}\sin\alpha,\tag{B27}$$

$$\Omega_z^{(1)}=\Omega_{z_1}^{(1)}\cos\alpha-\Omega_{x_1}^{(1)}\sin\alpha,\tag{B28}$$

and

$$\omega_x^{(2)}=\omega_{x_2}^{(2)}\cos\alpha-\omega_{z_2}^{(2)}\sin\alpha,\tag{B29}$$

$$\omega_z^{(2)}=\omega_{z_2}^{(2)}\cos\alpha+\omega_{x_2}^{(2)}\sin\alpha,\tag{B30}$$

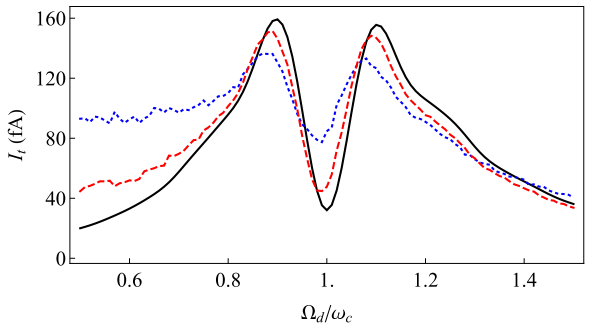

FIG. 8. (a)–(c) Leakage current I_t as a function of the driving Rabi frequency Ω_d/ω_c for an oscillating magnetic field with amplitude $b = 5.65\ \mu$T [$\Omega_c = (2\pi)\ 1$ MHz] at time $t = 1.5\ \mu$s, where solid, dashed, dotted lines represent the results simulated with $\Delta f = 0, 5, 10$ MHz and $\tau = 100$ ms, respectively. The other parameters are the same as Fig. 2 in the main text.

$$\Omega_x^{(2)}=\Omega_{x_2}^{(2)}\cos\alpha-\Omega_{z_2}^{(2)}\sin\alpha,\tag{B31}$$

$$\Omega_z^{(2)}=\Omega_{z_2}^{(2)}\cos\alpha+\Omega_{x_2}^{(2)}\sin\alpha.\tag{B32}$$

The Pauli matrices $\hat{s}_{x,z}^{(j)}$ are written in the following basis:

$$\begin{aligned}\left|\Uparrow^{(j)}\right\rangle&=\exp\left[-(-1)^{j+1}\,i\alpha\hat{s}_{y_j}^{(j)}/2\right]\left|\Uparrow_j^{(j)}\right\rangle\\ &=\cos(\alpha/2)\left|\Uparrow_j^{(j)}\right\rangle-(-1)^{j+1}\,i\sin(\alpha/2)\,\hat{s}_{y_j}^{(j)}\left|\Uparrow_j^{(j)}\right\rangle\\ &=\cos(\alpha/2)\left|\Uparrow_j^{(j)}\right\rangle+(-1)^{j+1}\sin(\alpha/2)\left|\Downarrow_j^{(j)}\right\rangle,\end{aligned}\tag{B33}$$

$$\begin{aligned}\left|\Downarrow^{(j)}\right\rangle&=\exp\left[-(-1)^{j+1}\,i\alpha\hat{s}_{y_j}^{(j)}/2\right]\left|\Downarrow_j^{(j)}\right\rangle\\ &=\cos(\alpha/2)\left|\Downarrow_j^{(j)}\right\rangle-(-1)^{j+1}\,i\sin(\alpha/2)\,\hat{s}_{y_j}^{(j)}\left|\Downarrow_j^{(j)}\right\rangle\\ &=\cos(\alpha/2)\left|\Downarrow_j^{(j)}\right\rangle-(-1)^{j+1}\sin(\alpha/2)\left|\Uparrow_j^{(j)}\right\rangle.\end{aligned}\tag{B34}$$

The eigenstates of $\hat{H}_0=(1/2)\left[\omega_x^{(1)}\hat{s}_x^{(1)}+\omega_z^{(1)}\hat{s}_z^{(1)}\right]+(1/2)\left[\omega_x^{(2)}\hat{s}_x^{(2)}+\frac{1}{2}\omega_z^{(2)}\hat{s}_z^{(2)}\right]$ are

$$|L_0\rangle=\cos(\gamma_1/2)\left|\Uparrow^{(1)}\right\rangle+\sin(\gamma_1/2)\left|\Downarrow^{(1)}\right\rangle,\tag{B35}$$

$$|L_1\rangle=-\sin(\gamma_1/2)\left|\Uparrow^{(1)}\right\rangle+\cos(\gamma_1/2)\left|\Downarrow^{(1)}\right\rangle,\tag{B36}$$

$$|R_0\rangle=\cos(\gamma_2/2)\left|\Uparrow^{(2)}\right\rangle+\sin(\gamma_2/2)\left|\Downarrow^{(2)}\right\rangle,\tag{B37}$$

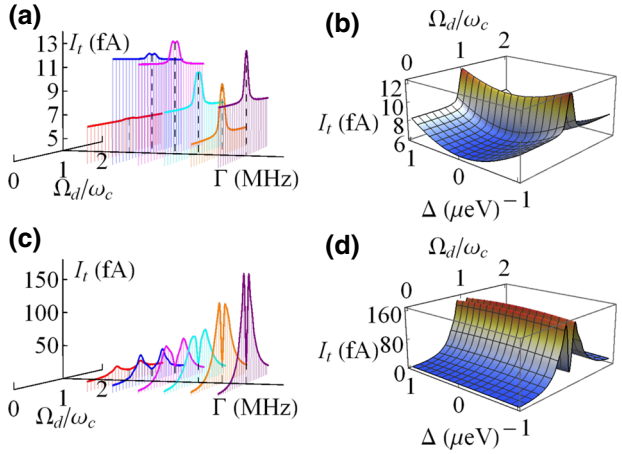

FIG. 9. (a),(c) Leakage current I_t as a function of the driving Rabi frequency Ω_d/ω_c at time $t = 1.5\ \mu$s for an oscillating magnetic field with frequency $\omega_c = (2\pi)\,5$ MHz and different amplitudes: (a) $b = 0.565\ \mu$T [$\Omega_c = (2\pi)\,0.1$ MHz] simulated with $J = (2\pi)\,10$ MHz; (c) $b = 5.65\ \mu$T [$\Omega_c = (2\pi)\,1$ MHz] simulated with $J = (2\pi)\,20$ MHz, in the presence of energy detuning $\Delta = 1\ \mu$eV, where the red, blue, magenta, cyan, orange, and purple lines represent the results simulated with the transition rate $\Gamma/(2\pi) = 10, 25, 75, 125, 250, 500$ MHz, respectively. (b),(d) Leakage current I_t as a function of the driving Rabi frequency Ω_d/ω_c and the energy detuning Δ at time $t = 1.5\ \mu$s for an oscillating magnetic field with frequency $\omega_c = (2\pi)\,5$ MHz and different amplitudes: (b) $b = 0.565\ \mu$T [$\Omega_c = (2\pi)\,0.1$ MHz] simulated with $J = (2\pi)\,10$ MHz; (d) $b = 5.65\ \mu$T [$\Omega_c = (2\pi)\,1$ MHz] simulated with $J = (2\pi)\,20$ MHz. The injection and ejection rates are $\Gamma_L = \Gamma_R = \Gamma = (2\pi)500$ MHz.

$$|R_1\rangle = -\sin(\gamma_2/2)\left|\Uparrow^{(2)}\right\rangle + \cos(\gamma_2/2)\left|\Downarrow^{(2)}\right\rangle, \tag{B38}$$

with $\cos\gamma_j = \omega_z^{(j)}/\omega_0^{(j)}$ and $\sin\gamma_j = \omega_x^{(j)}/\omega_0^{(j)}$. In this set of bases, $\hat{H}_{\rm tb}$ can be rewritten by

$$\begin{aligned}\hat{H}'_{\rm tb} = {}& \frac{1}{2}\omega_0^{(1)}\hat{S}_z^{(1)} + g_z^{(1)}\cos(\omega t)\,\hat{S}_z^{(1)} + g_x^{(1)}\cos(\omega t)\,\hat{S}_x^{(1)} \\ & + \Omega_{cz}\cos(\omega_c t)\,\hat{S}_z^{(1)} + \Omega_{cx}\cos(\omega_c t)\,\hat{S}_x^{(1)} + \frac{1}{2}\omega_0^{(2)}\hat{S}_z^{(2)} \\ & + g_z^{(2)}\cos(\omega t)\,\hat{S}_z^{(2)} + g_x^{(2)}\cos(\omega t)\,\hat{S}_x^{(2)},\end{aligned} \tag{B39}$$

with

$$\omega_0^{(j)} = \sqrt{\left(\omega_x^{(j)}\right)^2 + \left(\omega_z^{(j)}\right)^2}, \tag{B40}$$

$$g_z^{(j)} = \Omega_z^{(j)}\cos\gamma_j + \Omega_x^{(j)}\sin\gamma_j, \tag{B41}$$

$$g_x^{(j)} = \Omega_x^{(j)}\cos\gamma_j - \Omega_z^{(j)}\sin\gamma_j, \tag{B42}$$

$$\Omega_{cz} = \Omega_c\cos(\alpha - \gamma_1), \tag{B43}$$

$$\Omega_{cx} = \Omega_c\sin(\alpha - \gamma_1). \tag{B44}$$

In Fig. 7(a), it can be seen that for a certain value of $\delta_{KK'}$, it is possible to satisfy the condition $\omega_0^{(1)} = \omega_0^{(2)}$ by choosing an appropriate magnetic field B_x. For example, one shall apply $B_x = 207$ mT for $\delta_{KK'} = 0.2$ meV. And we plot the corresponding values of $\omega_{x,z}^{(j)}$ in Fig. 7(b), which depend on $\delta_{KK'}$ and B_x. The driving Rabi frequencies $g_x^{(j)}$ depend on the driven motion parameter $\delta_\theta^{(j)}$, see Fig. 7(c), which shows that $g_x^{(1)} = g_x^{(2)} = \Omega_d$ can be achieved by choosing appropriate $\delta_\theta^{(j)}$. Therefore, it is reasonable to consider the case of $\omega = \omega_0^{(1)} = \omega_0^{(2)}$. Using rotating-wave approximation under the conditions $\Omega_{cx}, \Omega_{cz} \ll \omega_c, g_x^{(j)}, g_z^{(j)} \ll \omega_0^{(j)}$, the total effective Hamiltonian can be simplified as follows:

$$\hat{H}_{sB} = \frac{1}{2}\Omega_d\hat{S}_x^{(1)} + \Omega_c\cos(\omega_c t)\,\hat{S}_z^{(1)} + \frac{1}{2}\Omega_d\hat{S}_x^{(2)}, \tag{B45}$$

where $\cos(\alpha - \gamma_1) \approx 1$ in the limit of $\omega_x^{(1)} \ll \omega_z^{(1)}$ and $\alpha \ll 1$.

Two electrons both in the right quantum dot can be considered as identical particles, thus the antisymmetric state can be written as

$$\left|S_g\right\rangle = \frac{1}{\sqrt{2}}\left(|R_1\rangle_2\,|R_0\rangle_2 - |R_0\rangle_2\,|R_1\rangle_2\right), \tag{B46}$$

where the subscript 1 and 2 denote the left and right quantum dot, respectively. As the tunneling between the left and right quantum dot does not change the electron state, the antisymmetric state of two electrons separated in the left and right quantum dot can be written as follows:

$$|S\rangle = \frac{1}{\sqrt{2}}\left(|R_1\rangle_1\,|R_0\rangle_2 - |R_0\rangle_1\,|R_1\rangle_2\right). \tag{B47}$$

Projecting Eq. (B47) into the basis of $\{|L_0\rangle\otimes|R_0\rangle, |L_0\rangle\otimes|R_1\rangle, |L_1\rangle\otimes|R_0\rangle, |L_1\rangle\otimes|R_1\rangle\}$, one can obtain

$$\begin{aligned}|S\rangle = {}& \frac{1}{\sqrt{2}}\beta_1\cos\left[(\zeta_1 - \zeta_2)/2\right]\left(|L_1\rangle\,|R_0\rangle - |L_0\rangle\,|R_1\rangle\right) \\ & + \frac{1}{\sqrt{2}}\beta_2\cos\left[(\zeta_1 - \zeta_2)/2\right]\left(|L_0\rangle\,|R_0\rangle + |L_1\rangle\,|R_1\rangle\right),\end{aligned} \tag{B48}$$

with

$$\langle L_0\,|R_0\rangle = \beta_1\cos\left[(\zeta_1 - \zeta_2)/2\right], \tag{B49}$$

$$\langle L_1\,|R_1\rangle = \beta_1\cos\left[(\zeta_1 - \zeta_2)/2\right], \tag{B50}$$

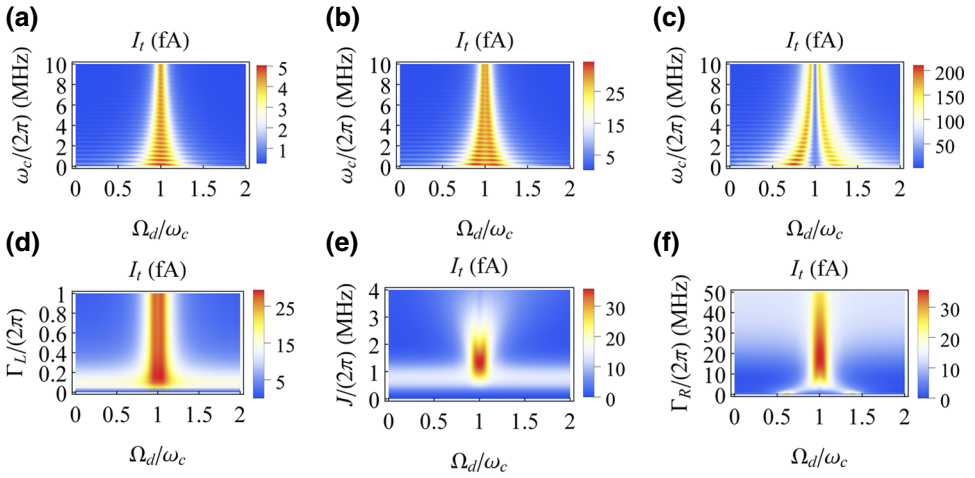

FIG. 10. (a)–(c) Leakage current I_t at time t as a function of the driving Rabi frequency Ω_d and the frequency ω_c of the oscillating magnetic field with different amplitudes: (a) $b_z = 0.565\ \mu$T [$\Omega_c = (2\pi)\,0.1$ MHz], (b) $b_z = 1.70\ \mu$T [$\Omega_c = (2\pi)\,0.3$ MHz], (c) $b_z = 5.65\ \mu$T [$\Omega_c = (2\pi)\,1$ MHz]. The other parameters are $J = (2\pi)\,2$ MHz and $\Gamma_L = \Gamma_R = (2\pi)\,8$ MHz. (d) Leakage current I_t at time t as a function of the driving Rabi frequency Ω_d and the electron injection rate Γ_L with $\omega_c = (2\pi)\,5$ MHz, $\Omega_c = (2\pi)\,0.3$ MHz, $J = (2\pi)\,2$ MHz and $\Gamma_R = (2\pi)\,8$ MHz. (e) Leakage current I_t at time t as a function of the driving Rabi frequency Ω_d and the tunneling rate J with $\omega_c = (2\pi)\,5$ MHz, $\Omega_c = (2\pi)\,0.3$ MHz and $\Gamma_L = \Gamma_R = (2\pi)\,8$ MHz. (f) Leakage current at time t I_t as a function of the driving Rabi frequency Ω_d and the electron ejection rate Γ_R with $\omega_c = (2\pi)\,5$ MHz, $\Omega_c = (2\pi)\,0.3$ MHz, $J = (2\pi)\,2$ MHz, and $\Gamma_L = (2\pi)\,8$ MHz. Taking one unpolarized electron located in the right quantum dot as the initial state. The time is set as $t = 1.5\ \mu$s.

$$\langle L_0\,|R_1\rangle = \beta_2 \cos\left[(\zeta_1 - \zeta_2)/2\right], \tag{B51}$$

$$\langle L_1\,|R_0\rangle = -\beta_2 \cos\left[(\zeta_1 - \zeta_2)/2\right], \tag{B52}$$

and

$$\beta_1 = \cos\left[(\gamma_1 - \gamma_2)/2 + \alpha\right], \tag{B53}$$

$$\beta_2 = \sin\left[(\gamma_1 - \gamma_2)/2 + \alpha\right]. \tag{B54}$$

As shown in Fig. 7(d), $\beta_2 \ll \beta_1$ is valid for a wide range of $\delta_{KK'}$ under the condition $\omega_0^{(1)} = \omega_0^{(2)}$. Therefore, after normalization, the antisymmetric state turns out to be

$$|S\rangle = \frac{1}{\sqrt{2}}\left(|L_1\rangle\,|R_0\rangle - |L_0\rangle\,|R_1\rangle\right). \tag{B55}$$

APPENDIX C: INFLUENCE OF DECOHERENCE

Gate-defined quantum dots in a carbon nanotube, suffers from decoherence mainly due to the hyperfine coupling with the environmental nuclear spins and the electric noise. The influence of nuclei may be mitigated by synthesizing a carbon nanotube with isotopically purified $^{12}CH_4$, allowing for the fabrication of devices without nuclear spins [23]. Under ideal conditions, the coherence time of a quantum dot in such an isotopically purified device is predicted to be of the order of seconds [48,49]. However, the charge noise due to the electric potential fluctuations modifies the parameters of the quantum dot, namely inducing fluctuations of the energy difference Δ between the singlet states $|S\rangle$ and $|S_g\rangle$ [40], as $H_\Delta = \Delta\,|S_g\rangle\,\langle S_g|$. In this section, we provide detailed analysis of the influence of decoherence on our proposed carbon nanotube quantum sensor.

1. Hyperfine coupling with nuclei

Nanotubes synthesized from natural hydrocarbons consist of 99% ^{12}C (nuclear spin $I = 0$) and 1% ^{13}C (nuclear spin $I = \frac{1}{2}$). The abundance of ^{13}C nuclei may be reduced to 0.01% or even lower by using isotopically purified CH_4 during the growth of nanotubes. The hyperfine coupling to the ^{13}C nuclear spins induces magnetic field noise on the confined quantum dot, leading to the slow fluctuation of frequency detuning of the encoded valley-spin qubit. The effective Hamiltonian for detecting a weakly oscillating magnetic field in the $(1,1)$ charge configuration, incorporating the noise in frequency detunings $\delta\omega_i\,(t)$ $(i = 1,2)$, can be written as

$$\begin{aligned}\hat{H}_{sB}^{*} = &\frac{1}{2}\left(\Omega_d \hat{S}_x^{(1)} + \delta\omega_1\,(t)\,\hat{S}_z^{(1)}\right)\\ &+ \frac{1}{2}\left(\Omega_d \hat{S}_x^{(2)} + \delta\omega_2\,(t)\,\hat{S}_z^{(2)}\right)\\ &+ \Omega_c \cos\left(\omega_c t\right)\hat{S}_z^{(1)}\end{aligned} \tag{C1}$$

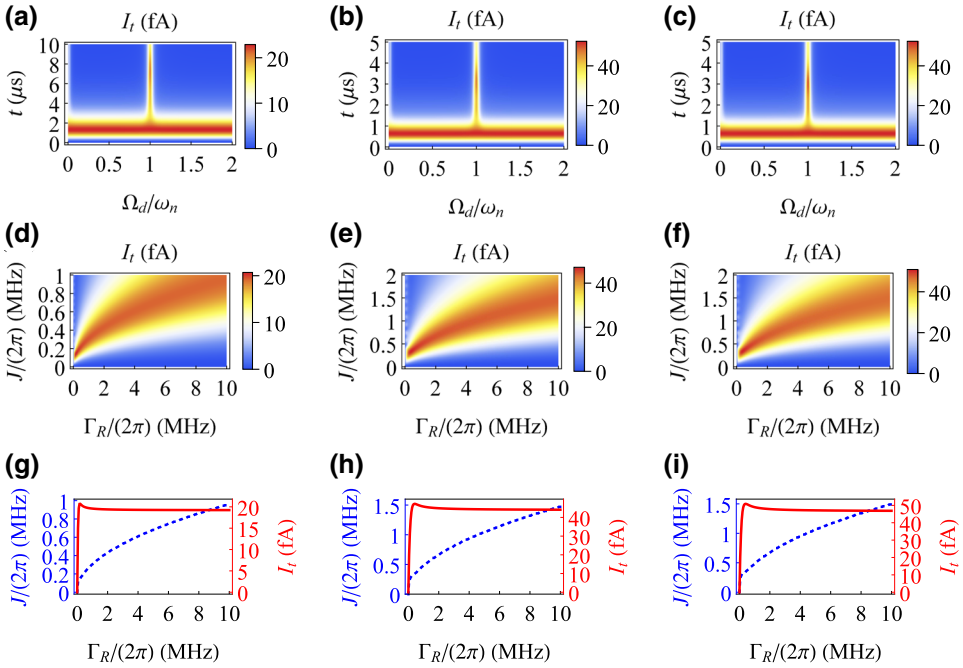

FIG. 11. (a)–(c) Leakage current I_t as a function of the driving Rabi frequency Ω_d/ω_n and the evolution time t for the nuclear spin ^{31}P (a) with $\Gamma_R = (2\pi)\,0.2$ MHz, $J = (2\pi)\,0.15$ MHz; the nuclear spin ^{19}F (b) with $\Gamma_R = (2\pi)\,0.4$ MHz, $J = (2\pi)\,0.35$ MHz; and the nuclear spin ^{1}H (c) with $\Gamma_R = (2\pi)\,0.4$ MHz, $J = (2\pi)\,0.35$ MHz, respectively, where $\omega_n = \gamma_n B$ is the Larmor frequency of nuclear spin. (d)–(f) Leakage current I_t as a function of the electron ejection rate Γ_R and the tunneling rate J on resonance of the nuclear spin ^{31}P (d) at time $t = 7$ μs, the nuclear spin ^{19}F (e) at time $t = 5$ μs and the nuclear spin ^{1}H (f) at time $t = 3$ μs. (g)–(i) The optimized leakage current (red solid lines) and the optimal parameters (blue dashed lines) of the electron ejection rate Γ_R and the tunneling rate J as shown in (d)–(f), respectively. In (a)–(i), the electron injection rate is $\Gamma_L = (2\pi)\,1$ MHz, the magnetic field is $B_x = 300$ mT and $B_z = 100$ mT. The other parameters are the same as Fig. 4 in the main text.

For numerical simulation, we assume that $\delta\omega_i\,(t)$ $(i = 1, 2)$ fulfills the Gaussian distribution

$$D\left(\delta\omega_i\right) = \frac{1}{\sqrt{2\pi}\,\Delta_f} e^{-\delta\omega_i^2/2\Delta_f^2}, \tag{C2}$$

and evolves following the Ornstein-Uhlenbeck process with

$$\delta\omega_i\,(t+dt) = \delta\omega_i\,(t)\,e^{-dt/\tau} + \left[\Delta_f^2\left(1 - e^{-2dt/\tau}\right)\right]^{1/2} n, \tag{C3}$$

where τ is the correlation time, which depends on the nuclear spin dynamics and relaxation, n represents a sample value of the unit normal random variable and $\Delta_f = \sqrt{2}/T_2^*$ is the standard deviation of $\delta\omega_i$. As T_2^* scales as $\sqrt{N/p}$, where N is the number of nuclei in the quantum dot and p is the isotopic fraction of ^{13}C, we can estimate Δf from the upper limit of T_2^* that is measured in an 99% isotopically purified ^{13}C nanotube quantum dot with $N \approx 7 \times 10^4$ nuclei in the interaction range [47]. For an isotopic fraction of ^{13}C of 0.0127% and 0.05%, we predict $\Delta f = 5$ and $\Delta f = 10$ MHz, respectively, with the same value of N. As shown in Fig. 8, the fluctuation of frequency detuning induced by the hyperfine coupling reduces the contrast of the resonance signal in a certain extent. Nevertheless, the influence can be well mitigated by isotopically engineering the nanotubes. The resonance signal of the oscillating magnetic field with larger amplitude demonstrates a more robust feature. Similar results can be obtained in the case of nanoscale magnetic resonance spectroscopy.

2. Charge noise

As the carbon nanotube quantum dot is gate defined, the electric noise modifies the energy levels of the quantum dot, i.e., inducing fluctuations of the energy detuning Δ between the singlet states $|S\rangle$ and $|S_g\rangle$ [40], as $H_\Delta = \Delta\,|S_g\rangle\,\langle S_g|$, the role of which in our scheme is mainly the suppression of effective tunneling. Thus, the influence may be compensated by choosing proper values of Γ_L, Γ_R, and J. This is in contrast to the dephasing effect on the coherence time of qubit involving the singlet state $|S_g\rangle$ in the (0,2) subspace [34], where the energy splitting of the qubit relies on the energy detuning Δ.

As shown in Figs. 9(a) and 9(c), when the energy detuning Δ up to 1μeV is considered, the resonant signal (dip or peak) of leakage current is degraded in the region with a small injection (ejection) rate of Γ ($\Gamma_L = \Gamma_R = \Gamma$). The influence of the energy detuning on the resonant signal

becomes negligible for larger but still reasonable rates Γ (with $\Gamma_L = \Gamma_R = \Gamma$). The results hold without relying on a large amplitude of the oscillating magnetic field. In addition, the resonance signal of the leakage current is tolerant to the energy detuning varying from -1 to 1 μeV when the transition rate is chosen as $\Gamma/(2\pi) = 500$ MHz [40], see Figs. 9(b) and 9(d). Therefore, improving the transition rate of the electron can efficiently compensate for the energy detuning between singlet states $|S\rangle$ and $|S_g\rangle$.

APPENDIX D: MORE DETAILS ON THE RESPONSE OF LEAKAGE CURRENT

1. Coupling to a weak oscillating signal field

As what we have presented in the main text, the leakage current always shows resonance features characterized by either a peak or a dip when the nanotube double quantum dot sensor couples with an oscillating magnetic field. The width of the resonance signal is critical for the spectra resolution. As shown in Figs. 10(a) and 10(c), it can be seen that the frequency of an oscillating magnetic field can also influence the width of the resonance signal. In particular, a smaller ratio Ω_c/ω_c leads to a sharper resonance signal.

In addition, there are another three important parameters Γ_L, J, and Γ_R that are involved in the process of electron transport directly. Γ_L (Γ_R) determines the rate at which electrons are continuously pumped into (out of) the left (right) quantum dot. J represents the electron tunneling rate between two quantum dots. Due to Coulomb blockade, these three parameters play an important role in the dynamic behavior of the leakage current when Pauli blockade is lifted by an oscillating magnetic field. As shown in Fig. 10(d), the leakage current is saturated when the injection rate Γ_L becomes large, because the residual electrons in the source lead are (Coulomb) blocked by the electron in the left quantum dot. As shown in Figs. 10(e) and 10(f), a large Γ_R and a suitable value of J leads to a more prominent leakage current. The dependence of leakage current on these parameters may help to optimize the performance of the proposed nanotube quantum sensor.

2. Identifying nucleus species

Based on the essential idea for the detection of an oscillating field, we propose to realize single molecule detection in the main text. A single molecule is usually characterized by different species of nuclear spins with multiple Larmor frequencies. For each individual nuclear spin, the magnetic moment determines not only the Larmor frequency in an external magnetic field, which indicates the driving Rabi frequency required to achieve a resonance signal but also the magnetic dipole-dipole coupling strength between the nuclear spin and the valley-spin qubit. As shown in Figs. 11(a)–11(c), once the driving Rabi frequency matches the Larmor frequency of each nuclear spin (^{31}P, ^{19}F, ^{1}H), the leakage current demonstrates a resonance feature. Given the same distance between the valley-spin qubit and the nuclear spin, the magnitude of leakage current induced by ^{31}P nuclear spin is much smaller than that of ^{31}F and ^{1}H nuclear spins due to its smaller magnetic moment. We remark that the values of parameters J and Γ_R have been optimized according to the results shown in Figs. 11(d)–11(f).

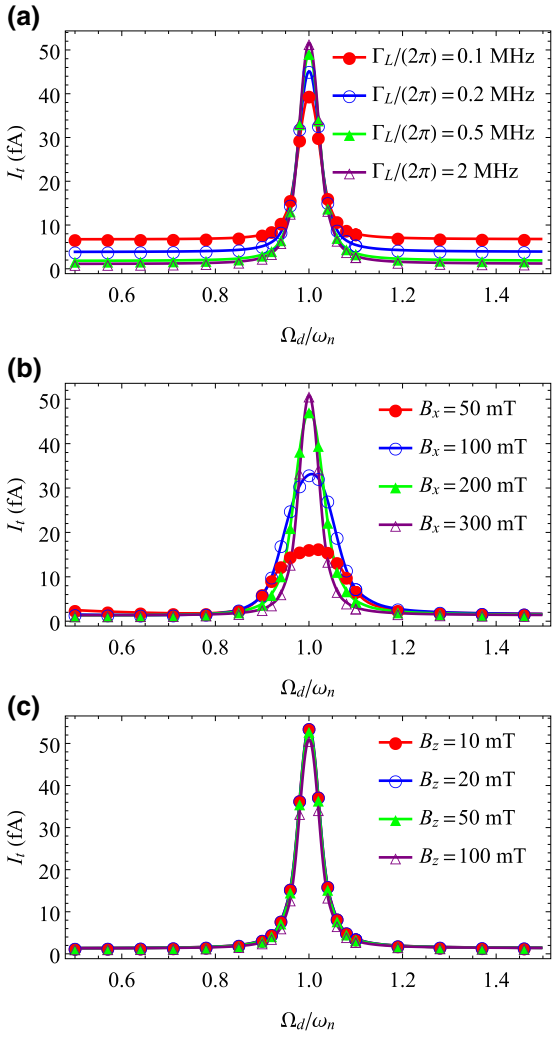

FIG. 12. Leakage current I_t as a function of the driving Rabi frequency Ω_d/ω_n for the nuclear spin ^{1}H, where $\omega_n = \gamma_n B$ is the Larmor frequency of nuclear spin. (a) Under the situations with different injection rate Γ_L, where $B_x = 300$ mT and $B_z = 100$ mT. (b) Under the situations with different magnetic field B_x, where $\Gamma_L = (2\pi)\,1$ MHz and $B_z = 100$ mT. (c) Under the situations with different magnetic field B_z, where $\Gamma_L = (2\pi)\,1$ MHz and $B_x = 300$ mT. In (a)–(c) $\Gamma_R = (2\pi)\,0.4$ MHz, $J = (2\pi)\,0.35$ MHz, and $t = 3$ μs. The other parameters are the same as Fig. 4 in the main text.

We also investigate the effect of the parameters Γ_L, B_x, B_z on the observed resonance signal. In Fig. 12(a), the leakage current on resonance increases with the electron

injection rate Γ_L up to a saturation value when $\Gamma_L/2\pi$ is about 1 MHz. In Figs. 12(b) and 12(c), we plot the leakage current for different values of transverse (B_x) and longitudinal (B_z) magnetic field components. It can be seen that the peak value of leakage current is almost independent on B_z, while it increases as B_x becomes larger.

[1] C. L. Degen, F. Reinhard, and P. Cappellaro, Quantum sensing, Rev. Mod. Phys. **89**, 035002 (2017).

[2] A. M. Armani, R. P. Kulkarni, S. E. Fraser, R. C. Flagan, and K. J. Vahala, Label-free, single-molecule detection with optical microcavities, Science **317**, 783 (2007).

[3] J. O. Arroyo and P. Kukura, Non-fluorescent schemes for single-molecule detection, imaging and spectroscopy, Nat. Photonics **10**, 11 (2015).

[4] J. Lee, N. Tallarida, X. Chen, L. Jensen, and V. A. Apkarian, Microscopy with a single-molecule scanning electrometer, Sci. Adv. **4**, eaat5472 (2018).

[5] D. R. Glenn, D. B. Bucher, J. Lee, M. D. Lukin, H. Park, and R. L. Walsworth, High-resolution magnetic resonance spectroscopy using a solid-state spin sensor, Nature **555**, 351 (2018).

[6] S. Schmitt, T. Gefen, F. M. Stürner, T. Unden, G. Wolff, C. Müller, J. Scheuer, B. Naydenov, M. Markham, S. Pezzagna, J. Meijer, I. Schwarz, M. Plenio, A. Retzker, L. P. McGuinness, and F. Jelezko, Submillihertz magnetic spectroscopy performed with a nanoscale quantum sensor, Science **356**, 832 (2017).

[7] I. Lovchinsky, A. O. Sushkov, E. Urbach, N. P. de Leon, S. Choi, K. De Greve, R. Evans, R. Gertner, E. Bersin, C. Müller, L. McGuinness, F. Jelezko, R. L. Walsworth, H. Park, and M. D. Lukin, Nuclear magnetic resonance detection and spectroscopy of single proteins using quantum logic, Science **351**, 836 (2016).

[8] F. Shi, Q. Zhang, P. Wang, H. Sun, J. Wang, X. Rong, M. Chen, C. Ju, F. Reinhard, H. Chen, J. Wrachtrup, J. Wang, and J. Du, Single-protein spin resonance spectroscopy under ambient conditions, Science **347**, 1135 (2015).

[9] C. Müller, X. Kong, J. M. Cai, K. Melentijević, A. Stacey, M. Markham, D. Twitchen, J. Isoya, S. Pezzagna, J. Meijer, J. F. Du, M. B. Plenio, B. Naydenov, L. P. McGuinness, and F. Jelezko, Nuclear magnetic resonance spectroscopy with single spin sensitivity, Nat. Commun. **5**, 4703 (2014).

[10] A. O. Sushkov, I. Lovchinsky, N. Chisholm, R. L. Walsworth, H. Park, and M. D. Lukin, Magnetic Resonance Detection of Individual Proton Spins Using Quantum Reporters, Phys. Rev. Lett. **113**, 197601 (2014).

[11] T. Staudacher, F. Shi, S. Pezzagna, J. Meijer, J. Du, C. A. Meriles, F. Reinhard, and J. Wrachtrup, Nuclear magnetic resonance spectroscopy on a (5-Nanometer)3 sample volume, Science **339**, 561 (2013).

[12] H. J. Mamin, M. Kim, M. H. Sherwood, C. T. Rettner, K. Ohno, D. D. Awschalom, and D. Rugar, Nanoscale nuclear magnetic resonance with a nitrogen-vacancy spin sensor, Science **339**, 557 (2013).

[13] J. Cai, F. Jelezko, and M. B. Plenio, Hybrid sensors based on colour centres in diamond and piezoactive layers, Nat. Commun. **5**, 4065 (2014).

[14] T. Zhang, G.-Q. Liu, W.-H. Leong, C.-F. Liu, M.-H. Kwok, T. Ngai, R.-B. Liu, and Q. Li, Hybrid nanodiamond quantum sensors enabled by volume phase transitions of hydrogels, Nat. Commun. **9**, 3188 (2018).

[15] H. Liu, M. B. Plenio, and J. Cai, Scheme for Detection of Single Molecule Radical Pair Reaction Using Spin in Diamond, Phys. Rev. Lett. **118**, 200402 (2017).

[16] M. W. Doherty, N. B. Manson, P. Delaney, F. Jelezko, J. Wrachtrup, and L. C. L. Hollenberg, The nitrogen-vacancy colour centre in diamond, Phys. Rep. **528**, 1 (2013).

[17] R. Schirhagl, K. Chang, M. Loretz, and C. L. Degen, Nitrogen-vacancy centers in diamond: Nanoscale sensors for physics and biology, Annu. Rev. Phys. Chem. **65**, 83 (2014).

[18] Y. Wu, F. Jelezko, M. B. Plenio, and T. Weil, Diamond quantum devices in biology, Angew. Chem. Int. Ed. **55**, 6586 (2016).

[19] J. Tisler, G. Balasubramanian, B. Naydenov, R. Kolesov, B. Grotz, R. Reuter, J.-P. Boudou, P. A. Curmi, M. Sennour, A. Thorel, M. Börsch, K. Aulenbacher, R. Erdmann, P. R. Hemmer, F. Jelezko, and J. Wrachtrup, Fluorescence and spin properties of defects in single digit nanodiamonds, ACS Nano **3**, 1959 (2009).

[20] T. Rosskopf, A. Dussaux, K. Ohashi, M. Loretz, R. Schirhagl, H. Watanabe, S. Shikata, K. M. Itoh, and C. L. Degen, Investigation of Surface Magnetic Noise by Shallow Spins in Diamond, Phys. Rev. Lett. **112**, 147602 (2014).

[21] B. A. Myers, A. Das, M. C. Dartiailh, K. Ohno, D. D. Awschalom, and A. C. Bleszynski Jayich, Probing Surface Noise with Depth-Calibrated Spins in Diamond, Phys. Rev. Lett. **113**, 027602 (2014).

[22] M. Kim, H. J. Mamin, M. H. Sherwood, K. Ohno, D. D. Awschalom, and D. Rugar, Decoherence of Near-Surface Nitrogen-Vacancy Centers Due to Electric Field Noise, Phys. Rev. Lett. **115**, 087602 (2015).

[23] E. A. Laird, F. Kuemmeth, G. A. Steele, K. Grove-Rasmussen, J. Nygård, K. Flensberg, and L. P. Kouwenhoven, Quantum transport in carbon nanotubes, Rev. Mod. Phys. **87**, 703 (2015).

[24] N. Rohling and G. Burkard, Universal quantum computing with spin and valley states, New J. Phys. **14**, 083008 (2012).

[25] A. Pályi and G. Burkard, Hyperfine-induced valley mixing and the spin-valley blockade in carbon-based quantum dots, Phys. Rev. B **80**, 201404 (2009).

[26] S. J. Chorley, G. Giavaras, J. Wabnig, G. A. C. Jones, C. G. Smith, G. A. D. Briggs, and M. R. Buitelaar, Transport Spectroscopy of an Impurity Spin in a Carbon Nanotube Double Quantum Dot, Phys. Rev. Lett. **106**, 206801 (2011).

[27] H. O. H. Churchill, F. Kuemmeth, J. W. Harlow, A. J. Bestwick, E. I. Rashba, K. Flensberg, C. H. Stwertka, T. Taychatanapat, S. K. Watson, and C. M. Marcus, Relaxation and Dephasing in a Two-Electron ^{13}**C** Nanotube Double Quantum Dot, Phys. Rev. Lett. **102**, 166802 (2009).

[28] F. Pei, E. A. Laird, G. A. Steele, and L. P. Kouwenhoven, Valley–spin blockade and spin resonance in carbon nanotubes, Nat. Nanotechnol. **7**, 630 (2012).

[29] S. Moriyama, T. Fuse, M. Suzuki, Y. Aoyagi, and K. Ishibashi, Four-Electron Shell Structures and an Interacting Two-Electron System in Carbon-Nanotube Quantum Dots, Phys. Rev. Lett. **94**, 186806 (2005).

[30] K. Grove-Rasmussen, S. Grap, J. Paaske, K. Flensberg, S. Andergassen, V. Meden, H. I. Jørgensen, K. Muraki, and T. Fujisawa, Magnetic-Field Dependence of Tunnel Couplings in Carbon Nanotube Quantum Dots, Phys. Rev. Lett. **108**, 176802 (2012).

[31] F. H. L. Koppens, C. Buizert, K. J. Tielrooij, I. T. Vink, K. C. Nowack, T. Meunier, L. P. Kouwenhoven, and L. M. K. Vandersypen, Driven coherent oscillations of a single electron spin in a quantum dot, Nature **442**, 766 (2006).

[32] S. Thiele, F. Balestro, R. Ballou, S. Klyatskaya, M. Ruben, and W. Wernsdorfer, Electrically driven nuclear spin resonance in single-molecule magnets, Science **344**, 1135 (2014).

[33] K. Flensberg and C. M. Marcus, Bends in nanotubes allow electric spin control and coupling, Phys. Rev. B **81**, 195418 (2010).

[34] E. A. Laird, F. Pei, and L. P. Kouwenhoven, A valley–spin qubit in a carbon nanotube, Nat. Nanotechnol. **8**, 565 (2013).

[35] F. H. L. Koppens, J. A. Folk, J. M. Elzerman, R. Hanson, L. H. W. van Beveren, I. T. Vink, H. P. Tranitz, W. Wegscheider, L. P. Kouwenhoven, and L. M. K. Vandersypen, Control and detection of singlet-triplet mixing in a random nuclear field, Science **309**, 1346 (2005).

[36] O. N. Jouravlev and Y. V. Nazarov, Electron Transport in a Double Quantum Dot Governed by a Nuclear Magnetic Field, Phys. Rev. Lett. **96**, 176804 (2006).

[37] K. Grove-Rasmussen, H. I. Jørgensen, T. Hayashi, P. E. Lindelof, and T. Fujisawa, A triple quantum dot in a single-wall carbon nanotube, Nano Lett. **8**, 1055 (2008).

[38] J. P. Lu, Novel Magnetic Properties of Carbon Nanotubes, Phys. Rev. Lett. **74**, 1123 (1995).

[39] G. Széchenyi and A. Pályi, Shape-sensitive Pauli blockade in a bent carbon nanotube, Phys. Rev. B **91**, 045431 (2015).

[40] G. Széchenyi and A. Pályi, Coulomb-blockade and Pauli-blockade magnetometry, Phys. Rev. B **95**, 035431 (2017).

[41] Y. Li, S. C. Benjamin, G. A. D. Briggs, and E. A. Laird, Electrically driven spin resonance in a bent disordered carbon nanotube, Phys. Rev. B **90**, 195440 (2014).

[42] F. Kuemmeth, S. Ilani, D. C. Ralph, and P. L. McEuen, Coupling of spin and orbital motion of electrons in carbon nanotubes, Nature **452**, 448 (2008).

[43] A. Pályi and G. Burkard, Spin-valley blockade in carbon nanotube double quantum dots, Phys. Rev. B **82**, 155424 (2010).

[44] M. C. Hels, B. Braunecker, K. Grove-Rasmussen, and J. Nygård, Noncollinear Spin-Orbit Magnetic Fields in a Carbon Nanotube Double Quantum Dot, Phys. Rev. Lett. **117**, 276802 (2016).

[45] J. M. Cai, B. Naydenov, R. Pfeiffer, L. P. McGuinness, K. D. Jahnke, F. Jelezko, M. B. Plenio, and A. Retzker, Robust dynamical decoupling with concatenated continuous driving, New J. Phys. **14**, 113023 (2012).

[46] R. Hanson, L. P. Kouwenhoven, J. R. Petta, S. Tarucha, and L. M. K. Vandersypen, Spins in few-electron quantum dots, Rev. Mod. Phys. **79**, 1217 (2007).

[47] H. O. H. Churchill, F. Kuemmeth, J. W. Harlow, A. J. Bestwick, E. I. Rashba, K. Flensberg, C. H. Stwertka, T. Taychatanapat, S. K. Watson, and C. M. Marcus, Relaxation and Dephasing in a Two-Electron ^{13}**C** Nanotube Double Quantum Dot, Phys. Rev. Lett. **102**, 166802 (2009).

[48] D. V. Bulaev, B. Trauzettel, and D. Loss, Spin-orbit interaction and anomalous spin relaxation in carbon nanotube quantum dots, Phys. Rev. B **77**, 235301 (2008).

[49] M. S. Rudner and E. I. Rashba, Spin relaxation due to deflection coupling in nanotube quantum dots, Phys. Rev. B **81**, 125426 (2010).

[50] B. M. Freeman, J. S. Schoenfield, and H. Jiang, Comparison of low frequency charge noise in identically patterned Si/SiO2 and Si/SiGe quantum dots, Appl. Phys. Lett. **108**, 253108 (2016).

[51] W. A. Coish and F. Qassemi, Leakage-current line shapes from inelastic cotunneling in the Pauli spin blockade regime, Phys. Rev. B **84**, 245407 (2011).

[52] N. S. Lai, W. H. Lim, C. H. Yang, F. A. Zwanenburg, W. A. Coish, F. Qassemi, A. Morello, and A. S. Dzurak, Pauli spin blockade in a highly tunable silicon double quantum dot, Sci. Rep. **1**, 110 (2011).

[53] R. Hanson, L. M. K. Vandersypen, L. H. W. van Beveren, J. M. Elzerman, I. T. Vink, and L. P. Kouwenhoven, Semiconductor few-electron quantum dot operated as a bipolar spin filter, Phys. Rev. B **70**, 241304 (2004).

[54] X. Tu and M. Zheng, A DNA-based approach to the carbon nanotube sorting problem, Nano Res. **1**, 185 (2008).

[55] H. K. Moon, C. I. Chang, D.-K. Lee, and H. C. Choi, Effect of nucleases on the cellular internalization of fluorescent labeled DNA-functionalized single-walled carbon nanotubes, Nano Res. **1**, 351 (2008).

[56] S. A. Gurvitz and Y. S. Prager, Microscopic derivation of rate equations for quantum transport, Phys. Rev. B **53**, 15932 (1996).

[57] X.-Q. Li, J. Luo, Y.-G. Yang, P. Cui, and Y. Yan, Quantum master-equation approach to quantum transport through mesoscopic systems, Phys. Rev. B **71**, 205304 (2005).